nature genetics

Article

https://doi.org/10.1038/s41588-023-01307-z

Pharmacological disruption of mSWI/SNF complex activity restricts SARS-CoV-2 infection

Received: 11 August 2022

Accepted: 23 January 2023

Published online: 9 March 2023

Check for updates

Jin Wei[1,2,21], Ajinkya Patil[3,4,5,21], Clayton K. Collings[3,4], Mia Madel Alfajaro[1,2], Yu Liang[6,7], Wesley L. Cai[8], Madison S. Strine[1,2], Renata B. Filler[1,2], Peter C. DeWeirdt[9], Ruth E. Hanna[9], Bridget L. Menasche[1,2], Arya Ökten[1,2], Mario A. Peña-Hernández[1,2], Jon Klein[2], Andrew McNamara[1,2], Romel Rosales[10,11], Briana L. McGovern[10,11], M. Luis Rodriguez[10,11], Adolfo García-Sastre[10,11,12,13,14], Kris M. White[10,11], Yiren Qin[15,16,17], John G. Doench[9], Qin Yan[18,19], Akiko Iwasaki[18,19,20], Thomas P. Zwaka[15,16,17], Jun Qi[6,7], Cigall Kadoch[3,4,20,22] ✉ & Craig B. Wilen[1,2,19,22] ✉

Identification of host determinants of coronavirus infection informs mechanisms of viral pathogenesis and can provide new drug targets. Here we demonstrate that mammalian SWItch/Sucrose Non-Fermentable (mSWI/SNF) chromatin remodeling complexes, specifically canonical BRG1/BRM-associated factor (cBAF) complexes, promote severe acute respiratory syndrome coronavirus 2 (SARS-CoV-2) infection and represent host-directed therapeutic targets. The catalytic activity of SMARCA4 is required for mSWI/SNF-driven chromatin accessibility at the *ACE2* locus, *ACE2* expression and virus susceptibility. The transcription factors HNF1A/B interact with and recruit mSWI/SNF complexes to *ACE2* enhancers, which contain high HNF1A motif density. Notably, small-molecule mSWI/SNF ATPase inhibitors or degraders abrogate angiotensin-converting enzyme 2 (ACE2) expression and confer resistance to SARS-CoV-2 variants and a remdesivir-resistant virus in three cell lines and three primary human cell types, including airway epithelial cells, by up to 5 logs. These data highlight the role of mSWI/SNF complex activities in conferring SARS-CoV-2 susceptibility and identify a potential class of broad-acting antivirals to combat emerging coronaviruses and drug-resistant variants.

While coronavirus disease 2019 vaccines are effective, inadequate vaccination rates, breakthrough infections and viral evolution highlight the need for new antiviral strategies against current and emerging coronaviruses[1]. Enhanced understanding of virus–host interactions at the cellular and molecular levels is critical for the development of both prophylactic and therapeutic approaches[2]. Currently authorized direct-acting antivirals target the viral polymerase (remdesivir and molnupiravir) and viral protease (paxlovid). However, viral resistance, drug–drug interactions and variable efficacy highlight the need for new drug classes with broad activity[3–7]. Host-directed therapeutics provide a particularly promising approach given the potentially higher barrier to drug resistance, increased breadth of activity across coronavirus variants and species and the likelihood of synergy with direct-acting antiviral drugs[8–10].

A full list of affiliations appears at the end of the paper. ✉e-mail: cigall_kadoch@dfci.harvard.edu; craig.wilen@yale.edu

Coronavirus entry is mediated by the interaction of the viral spike (S) glycoprotein with a cellular receptor. Three of the seven human coronaviruses including the severe acute respiratory syndrome (SARS)-related beta-coronaviruses (sarbecoviruses) SARS-CoV-1 and SARS-CoV-2, as well as the common cold coronavirus HCoV-NL63, use angiotensin-converting enzyme 2 (ACE2) as a receptor, whereas Middle East respiratory syndrome coronavirus (MERS-CoV) uses dipeptidyl peptidase-4 (DPP4)[11–14]. The S glycoprotein requires proteolytic processing before entry, which can be mediated by several proteases including transmembrane protease serine 2 (TMPRSS2) and the endosomal protease cathepsin L[15–18]. On viral entry, viral RNA is released into the cytoplasm where it is translated and establishes viral replication and transcription complexes before assembling and budding[19–21].

We recently performed a genome-wide CRISPR–Cas9-based screen to identify host genes essential for highly pathogenic coronavirus infection in African green monkey Vero E6 cells[22]. Many top proviral genes for SARS-CoV-2 encoded subunits of the mammalian SWItch/Sucrose Non-Fermentable (mSWI/SNF) complex: *SMARCA4*, *ARID1A*, *DPF2*, *SMARCE1*, *SMARCB1* and *SMARCC1* (ref. [22]). These subunit genes have also been identified in other CRISPR screens performed across several different human cell lines[23–25]. mSWI/SNF or BRG1/BRM-associated factor (BAF) complexes are ATP-dependent chromatin remodeling complexes that modulate genomic architecture and gene expression[26–28]. mSWI/SNF complexes are highly conserved across eukaryotes and form three subcomplexes, each with distinct subunit composition, genomic localization properties, nucleosome binding interactions and functions: canonical BAF (cBAF or BAF), polybromo-associated BAF (PBAF) and noncanonical BAF (ncBAF) complexes[29–31]. All mSWI/SNF complexes contain an ATPase subunit, SMARCA4 or SMARCA2 (also known as BRG1 and BRM, respectively), and an array of both shared and complex-specific subunits[29,32]. The cBAF (or BAF) subcomplex is the most stoichiometrically abundant mSWI/SNF complex in mammalian cells, localizing primarily to *cis*-regulatory enhancer elements on the genome[33–38]. As a family, mSWI/SNF complexes represent the most frequently mutated chromatin regulatory entity in human cancer, with >20% of human cancers bearing mutations, including several rare cancers in which mutations are uniformly driving[26,27,36,39,40]. Further, mSWI/SNF genes are frequently perturbed in neurodevelopmental disorders[35,41]. Importantly, well-tolerated and orally bioavailable small-molecule inhibitors and degraders targeting mSWI/SNF family complexes have been recently developed and are currently in human phase I clinical trials across a range of oncology-centered indications (NCT04879017, NCT04891757). However, the mechanism by which mSWI/SNF complexes mediate SARS-CoV-2 infection is unknown.

In this study, we demonstrate that functional mSWI/SNF complexes are required for SARS-CoV-2 infection and viral entry in cell lines and three primary human cell types. We show that mSWI/SNF complex catalytic activity is essential for DNA accessibility at the *ACE2* locus and *ACE2* expression. Enhanced BAF complex targeting to the *ACE2* locus is mediated by the transcription factors HNF1A/B, which bind BAF complexes and direct them to sites of high local HNF1A/B motif density. Finally, inhibition of mSWI/SNF ATP-dependent chromatin remodeling activity using three different SMARCA4/2-specific orally bioavailable small-molecule inhibitors and degraders attenuates *ACE2* expression and reduces infection of numerous SARS-CoV-2 variants. SMARCA4 inhibitors also inhibit infection of a remdesivir-resistant SARS-CoV-2, highlighting the utility for new antiviral drug classes. Notably, mSWI/SNF complexes do not regulate mouse *ACE2* expression, suggesting species-specific regulation of ACE2. Together, these data implicate mSWI/SNF complexes as critical regulators of SARS-CoV-2 infection and new host-directed therapeutic targets.

Results

cBAF is required for SARS-CoV-2 infection

Our previous screens identified genes encoding mSWI/SNF complex subunits as critical for SARS-CoV-2 infection, most notably, those subunits corresponding to the cBAF complex[22,29,42] (Fig. 1a and Extended Data Fig. 1a,b). To determine which of the three mSWI/SNF family complexes regulate SARS-CoV-2 infection, we generated polyclonal knockout cells of SMARCA4 (shared subunit), ARID1A (cBAF-specific subunit), ARID2 (PBAF-specific subunit) and BRD9 (ncBAF-specific subunit) and ACE2 as a positive control in Vero E6 cells using CRISPR–Cas9. We challenged cells with a replication-competent infectious clone of SARS-CoV-2 expressing the fluorescence-based reporter mNeonGreen (SARS-CoV-2-mNeonGreen) and quantified the frequency of infected cells by microscopy[43]. Genetic inactivation of SMARCA4 and ARID1A conferred resistance to SARS-CoV-2-mNG relative to a control single-guide RNA (sgRNA). Inactivation of ARID2 and BRD9 did not reduce infection (Fig. 1b). Consistent with this, disruption of SMARCA4 and ARID1A, but not ARID2 and BRD9, reduced the frequency of SARS-CoV-2-induced cell death (Extended Data Fig. 1c). Similarly, inactivation of SMARCA4 and ARID1A, but not ARID2 or BRD9, inhibited SARS-CoV-2 pseudovirus entry (Extended Data Fig. 1d,e). Collectively, these data demonstrate that the cBAF complex, marked by the complex-specific subunit ARID1A, is required for SARS-CoV-2 entry into cells.

To assess whether the proviral role of SMARCA4 is restricted to Vero E6 cells, we generated polyclonal SMARCA4 knockout cells in human Huh7.5 and Calu-3 cells, derived from human liver and lung, respectively. Both cell lines endogenously express ACE2 and support SARS-CoV-2 infection. SMARCA4 disruption reduced SARS-CoV-2-induced cell death, SARS-CoV-2 replication and pseudovirus entry in Huh7.5 cells (Extended Data Fig. 2a–e). Similarly, disruption of SMARCA4 in Calu-3 cells conferred protection from SARS-CoV-2-induced cell death and reduced pseudovirus entry (Extended Data Fig. 2f,g). These findings demonstrate a conserved role for ATPase-competent cBAF across cell types and primate species.

cBAF ATPase activity enables SARS-CoV-2 infection

SMARCA4, the catalytic subunit of mSWI/SNF complexes, most of which associates with cBAF, was second only to ACE2 in our CRISPR screens[22]. We generated four independent single-cell SMARCA4 knockout clones in Vero E6 cells using CRISPR–Cas9 and confirmed knockout efficiency by western blot (Extended Data Fig. 3a). All four SMARCA4 knockout clones were resistant to SARS-CoV-2-induced cell death, SARS-CoV-2 replication and pseudovirus entry (Extended Data Fig. 3b–d). To test whether the observed phenotypes resulted from the absence of SMARCA4 catalytic activity (rather than removal of the five-subunit ATPase module of BAF complexes that SMARCA4 nucleates[29]), we reintroduced wild-type (WT) SMARCA4, an ATPase-dead mutant (K785R) or empty vector control into SMARCA4 knockout cells (clone no. 3) and confirmed expression by western blot (Fig. 1c)[34,44,45]. mSWI/SNF complexes are essential for organism survival and mouse early development; loss of SMARCA4 in mice is embryonic lethal[46–48]. All four SMARCA4 knockout clones exhibited similar proliferation kinetics to WT cells demonstrating that SMARCA4 is not essential for Vero E6 cell replication or viability (Extended Data Fig. 3e). Importantly, reintroduction of WT SMARCA4, but not the K785R mutant, rescued virus replication in knockout cells (Fig. 1d). Similarly, we observed an approximate 3-log reduction of viral replication in SMARCA4 knockout and K785R catalytically inactive cells. This was rescued by complementation with WT SMARCA4 (Fig. 1e).

Next, we asked whether the proviral role of SMARCA4 was specific to SARS-CoV-2. We infected cells with either SARS-CoV-2, a bat coronavirus HKU5 expressing the SARS-CoV-1 S protein (HKU5-SARS-CoV-1-S), or MERS-CoV. The catalytic activity of SMARCA4 was necessary for virus-induced cell death from both SARS-CoV-2 and HKU5-SARS-CoV-1.

https://doi.org/10.1038/s41588-023-01307-z

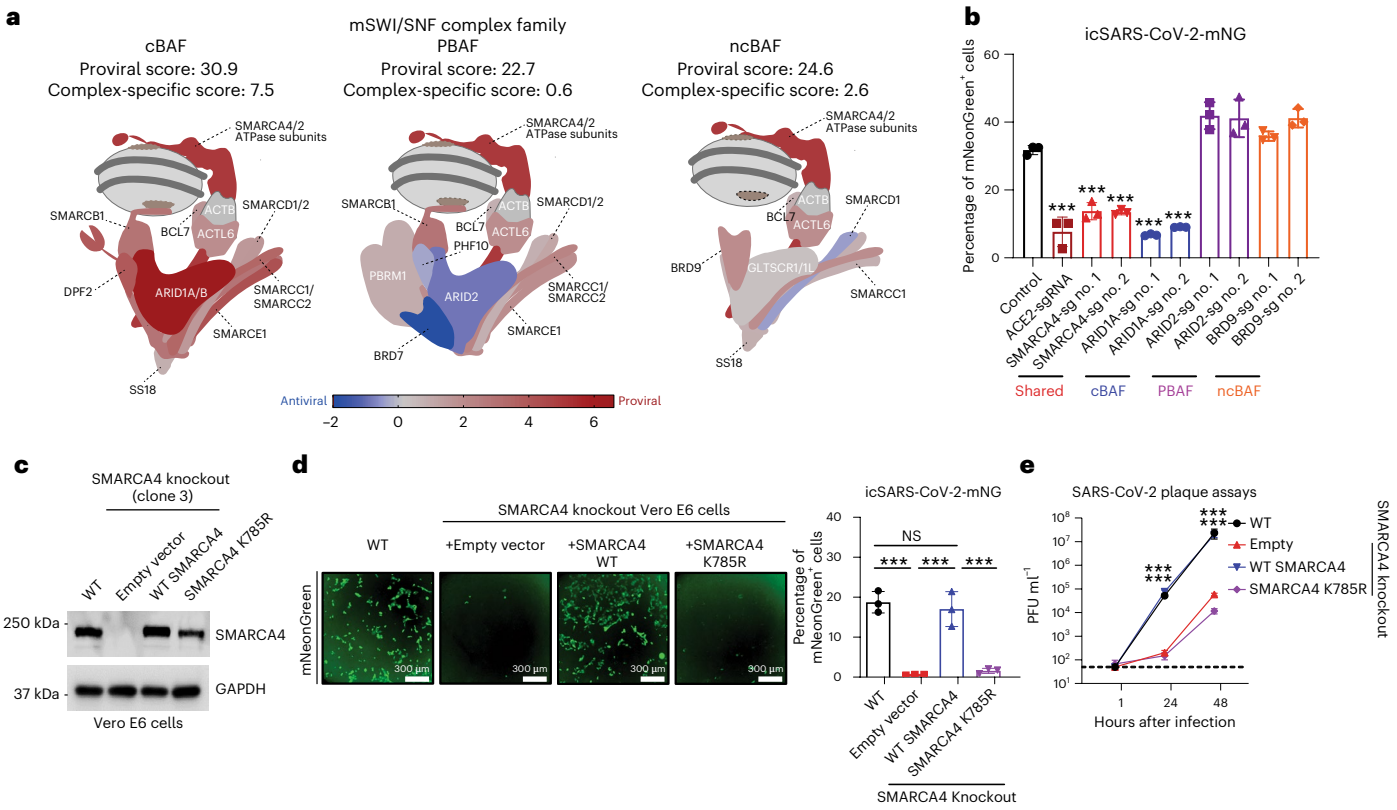

Fig. 1 | ATPase activity-competent mSWI/SNF complexes are essential for SARS-CoV-2 infection. a, Schematic of the three mSWI/SNF family complexes, cBAF, PBAF and ncBAF, with subunits colored according to scores in the Vero E6 SARS-CoV-2 CRISPR–Cas9 screen. The average proviral *z*-scores for each complex are shown. Complex-specific scores represent the sum of two complex-specific subunits, one core subunit and one reader subunit. **b**, Bar graph depicting the percentage of mNeonGreen-expressing Vero E6 cells (control cells or those with polyclonal CRISPR-mediated knockout of shared or unique mSWI/SNF subunits or ACE2) after infection by icSARS-CoV-2-mNG at an MOI of 1. **c**, Immunoblot performed in SMARCA4 knockout Vero E6 cells reconstituted with empty vector, WT SMARCA4 or SMARCA4 ATPase-dead mutant (K785R). **d**, SMARCA4 knockout-complemented and WT Vero E6 cells were infected with icSARS-CoV-2-mNG at an MOI of 1. Infected cells were imaged via fluorescence microscopy (left); mNeonGreen-expressing cell frequency was measured 2 d after infection (right). **e**, SMARCA4 knockout-complemented and WT Vero E6 cells were infected with SARS-CoV-2 at an MOI of 0.1. Virus titer was measured by plaque assay. PFU, plaque-forming unit. **f**, SMARCA4 knockout-complemented and WT Vero E6 cells were infected with SARS-CoV-2 (left), HKU5-SARS-CoV-1-S (middle) and MERS-CoV (right) at an MOI of 0.2. Cell viability relative to a mock-infected control was measured 3 d after infection with CellTiter-Glo (CTG). RLUs, relative light units. **g**, SMARCA4 knockout-complemented and WT Vero E6 cells were infected with VSV pseudovirus (VSVpp): VSVpp-VSV-G; VSVpp-SARS-CoV-2-S (left), VSVpp-SARS-CoV-1-S (middle) and VSVpp-MERS-CoV-S (right). Luciferase relative to the VSVpp-VSV-G control was measured 1 d after infection. Data in **b** and **d**–**g** were analyzed by one-way ANOVA with Tukey's multiple comparison test. The mean ± s.e.m. are shown. $^{**}P < 0.01$, $^{***}P < 0.001$, NS, not significant. $n = 3$ biological replicates. Data in **c** are representative one of three independent experiments.

In contrast, MERS-CoV-induced cell death was independent of SMARCA4 (Fig. 1f). In agreement with these findings, pseudovirus assays indicated that the ATPase activity of SMARCA4 is essential for viral entry of SARS-CoV-2 and SARS-CoV-1 but not MERS-CoV (Fig. 1g). These data demonstrate that SMARCA4 specifically promotes sarbecovirus infection in an ATPase activity-dependent manner.

cBAF regulates ACE2 levels and is essential for viral entry

We next sought to define the mechanism underpinning the essentiality of mSWI/SNF, specifically cBAF complexes, in SARS-CoV-2 infection. We performed genome-wide localization studies using CUT&Tag (C&T)[49] and DNA accessibility profiling using assay for transposase chromatin with sequencing (ATAC–seq)[50,51] in Vero E6 SMARCA4 knockout cells

https://doi.org/10.1038/s41588-023-01307-z

rescued with empty vector, WT SMARCA4 or the SMARCA4 K785R ATPase-dead mutant (Fig. 2a). Rescue of WT SMARCA4 resulted in increased numbers of BAF complex peaks and ATAC–seq-determined accessible peaks, as expected from previous studies performed in other cellular contexts[34] (Extended Data Fig. 4a–d). Integration and clustering analyses of these datasets enabled us to define three clusters of genomic sites including: those unoccupied by BAF complexes in all conditions (cluster 1); those with moderate gains in BAF complex occupancy and accessibility on SMARCA4 rescue (cluster 2); and those with substantial gains in BAF targeting and accessibility after expression of only WT SMARCA4 but not the catalytically dead SMARCA4 K785R mutant (ATPase activity-dependent sites) or empty vector control (cluster 3) (Fig. 2b,c). These ATPase activity-dependent sites were largely localized to sites distal to transcription start sites (TSS) and resulted

Fig. 2 | Top-ranked sites of ATPase-active BAF complex occupancy and DNA accessibility include *ACE2*. **a**, Immunoblot performed on nuclear extract (input) and anti-V5 immunoprecipitates from SMARCA4 knockout Vero E6 cells expressing either empty vector, WT V5-SMARCA4 or V5-SMARCA4 K785R. **b**, Heatmap and clustering analysis performed on the merged BAF complex (SMARCA4, SMARCC1 and ARID1A), H3K27ac occupancies ($n = 1$) and ATAC–seq ($n = 2$ biological replicates) peaks performed in Vero E6 cells rescued with the conditions shown in **a**, grouped into three clusters. **c**, Metaplots of SMARCA4 occupancy (C&T) and ATAC–seq peaks at WT SMARCA4-dependent sites (cluster 3). **d**, Distance to TSS distribution of C&T and ATAC–seq merged peaks for all conditions across clusters 1–3 from **b**. **e**, Cumulative distribution function plot reflecting genes nearest to SMARCC1 gained sites in SMARCA4 knockout cells rescued with WT SMARCA4 versus empty vector in cluster 3 from **b**; the top one-tenth fraction reflects genes associated with the top changed sites; sites highlighted in red indicate genes that scored as proviral determinants in the CRISPR screen. **f**, ATAC–seq and C&T tracks at the *ACE2* locus in SMARCA4 knockout Vero E6 cells rescued with empty vector, WT SMARCA4 or SMARCA4 K785R. **g**, Reads per kilobase of transcript per million reads mapped (RPKM) levels for *ACE2* in Vero E6 cells across the conditions shown ($n = 2$ biological replicates). The *P* values shown were calculated in edgeR using a quasi-likelihood negative binomial test. **h**, Volcano plots reflecting gene expression changes (RNA-seq) ($n = 2$ biological replicates) between the conditions shown. **i**, Overexpression of hACE2 in SMARCA4 knockout Vero E6 cells. **j**, VSVpp-based pseudovirus entry assay and plaque assays in WT Vero E6 cells and SMARCA4 knockout cells rescued with human ACE2. Data in **a** and **i** are representative of one of three independent experiments. Data in **j** were analyzed using a one-way ANOVA with Tukey's multiple comparisons test. The mean ± s.e.m. are shown. $^{**}P < 0.01$, $^{***}P < 0.001$, $n = 3$ biological replicates. The dashed line indicates limit of detection.

in the establishment of the H3K27ac and H3K4me1 chromatin marks, highlighting their potential role in mediating enhancer accessibility and activation (Fig. 2d and Extended Data Fig. 4e).

We next wanted to identify the most highly increased sites of BAF complex targeting and DNA accessibility within cluster 3 as a strategy to identify gene loci that may underpin the requirement for BAF complexes in SARS-CoV-2 infection. We ranked de novo BAF complex target sites (SMARCC1, SMARCA4 or ARID1A-gained sites) in SMARCA4 knockout cells rescued with WT SMARCA4 versus empty vector within cluster 3 and identified genes closest to these sites. This strategy led us to identify *ACE2* as a top-regulated locus (Fig. 2e). Notably, a number of additional genes localized to SMARCA4-dependent genomic regions were those found to mediate viral infection in our CRISPR screen along with *ACE2*, such as *SLC4A4* and *HNF1A* (Fig. 2e and Extended Data Fig. 4f), thus suggesting that mSWI/SNF complexes regulate a coronavirus susceptibility gene expression axis. We identified three putative enhancer sites, two distal and one proximal, and the promoter of *ACE2*, for which BAF complex occupancy and resulting DNA accessibility depended on the catalytic activity of SMARCA4 (Fig. 2f). Importantly, WT SMARCA4 was required for *ACE2* expression in Vero E6 cells (Fig. 2g,h). Notably, among the 236 transcripts that were dependent on ATPase-competent BAF complexes, three genes, *ACE2*, *SLC4A4* and *HNF1A*, overlapped with screening hits and were dependent on WT SMARCA4 for BAF complex targeting and genomic accessibility (Fig. 2e,h and Extended Data Fig. 4f–i). Taken together, these data underscore the critical role for ATPase-competent BAF complexes in regulating the accessibility of genes critical for SARS-CoV-2 infection, particularly the *ACE2* locus.

Finally, given that *ACE2* was among the most highly regulated genes upon SMARCA4 deletion (Fig. 2h and Extended Data Fig. 4j,k), we sought to determine if SARS-CoV-2 infectivity could be rescued in SMARCA4 knockout cells after rescue with human recombinant ACE2 (hACE2). Indeed, lentiviral expression of hACE2 in SMARCA4 knockout Vero E6 cells rescued SARS-CoV-2 infectivity as assessed by pseudovirus entry and plaque assay (Fig. 2i,j), underscoring that BAF-mediated regulation of ACE2 specifically is responsible for the pro-SARS-CoV-2 phenotype observed.

Enhanced cBAF complex targeting at ACE2 is mediated by HNF1A

We next sought to determine the mechanism by which the *ACE2* locus is regulated by the BAF complex. We performed motif analyses using HOMER v4.9 and MEME on the ATPase activity-dependent sites (cluster 3; Fig. 2b–d) to determine whether specific DNA motifs dominated these genomic regions. Indeed, motifs corresponding to the transcription factors HNF1A and HNF1B were highly enriched (Fig. 3a). Further, HNF1A (but not HNF1B) messenger RNA (mRNA) and protein levels were dependent on SMARCA4 in Vero E6 cells, suggesting that the nuclear abundance of HNF1A and its subsequent targeting to its cognate motifs is controlled by BAF complex activity (Fig. 3b,c and Extended Data Fig. 5a).

Given that the ATPase-dependent sites, including the *HNF1A* gene locus itself, showed the greatest enrichment of HNF1 motifs, we next sought to define the potential role for HNF1A and HNF1B factors in directing BAF complex occupancy and activity to genomic sites such as the *ACE2* locus. To do this, we generated HNF1A and HNF1B knockout Vero E6 cells and confirmed significant reduction of both *ACE2* mRNA and protein levels (Fig. 3d). Notably, genetic depletion of either HNF1A or HNF1B decreased SARS-CoV-2 infection in Vero E6 cells, as measured by mNeonGreen, plaque assays and pseudovirus entry assays (Fig. 3e–g). We confirmed these results in human Huh7.5 cells (Extended Data Fig. 5b–e).

Fig. 3 | HNF1A–BAF complex binding cooperates with high motif density at the *ACE2* locus to regulate *ACE2* expression. **a**, Transcription factor motif enrichment analysis at BAF-gained sites (cluster 3). **b**, Transcription factor motif enrichment at BAF-occupied gained sites after rescue of Vero E6 SMARCA4 knockout cells with WT SMARCA4 plotted against $\log_2$ fold change of the transcript levels of the transcription factors (empty vector versus WT SMARCA4 conditions). HNF1A and HNF1B are circled in red. **c**, Immunoblot of HNF1A/B across WT Vero E6 and SMARCA4 knockout cells rescued with empty vector, WT SMARCA4 or SMARCA4 K785R. **d**, *ACE2* expression in HNF1A and HNF1B knockout Vero E6 cells measured by RT–qPCR (left) and immunoblot (right). **e**, WT and HNF1A/B knockout Vero E6 cells were infected with icSARS-CoV-2-mNG at an MOI of 1. The frequency of infected cells was measured using mNeonGreen expression 2 d after infection. **f**, Vero E6 cells were infected with SARS-CoV-2 at an MOI of 0.1. Virus production was measured by plaque assays. **g**, HNF1A and HNF1B knockout Vero E6 cells were infected with SARS-CoV-2 pseudovirus. Luciferase relative to VSVpp-VSV-G control was measured 1 d after infection. **h**, Coimmunoprecipitation of endogenous SMARCA4 and HNF1A in nuclear extracts isolated from Vero E6 cells. **i**, HNF1 dimerization and association studies in WT and SMARCA2/4 double-knockout HEK 293T cells. **j**, Heatmap of SMARCA4 and SMARCC1 merged C&T ($n = 1$) and ATAC–seq ($n = 2$) peaks in control and HNF1A knockout Vero E6 cells, divided into three clusters. **k**, Bar graph depicting the fraction of sites with an HNF1 motif near cluster A (lost sites), cluster B (gained sites) and cluster C (unchanged sites) from **j**. **l**, Normalized gene rank of genes closest to cluster A sites plotted against the number of HNF1 motifs per gene at cluster A sites; selected genes within the top 10% of sites regulated by HNF1A are shown. **m**, C&T and ATAC–seq tracks at the *ACE2* locus in control and HNF1A knockout Vero E6 cells. The data in **c**, **d**, **h** and **i** are representative of one of three independent experiments. The data in **d**–**g** were analyzed using a one-way ANOVA with Tukey's multiple comparisons test. The mean ± s.e.m. are shown. $^{***}P < 0.001$, $n = 3$ biological replicates.

https://doi.org/10.1038/s41588-023-01307-z

We next asked whether HNF1A, HNF1B or both could bind BAF complexes. To evaluate this, we expressed human influenza hemagglutinin (HA)-tagged HNF1A and HNF1B in HEK 293T cells and performed immunoprecipitation assays. Notably, while HNF1A and HNF1B were expressed at comparable levels, immunoprecipitation of SMARCA4, and hence the BAF complexes, captured HA-HNF1A but not HA-HNF1B.

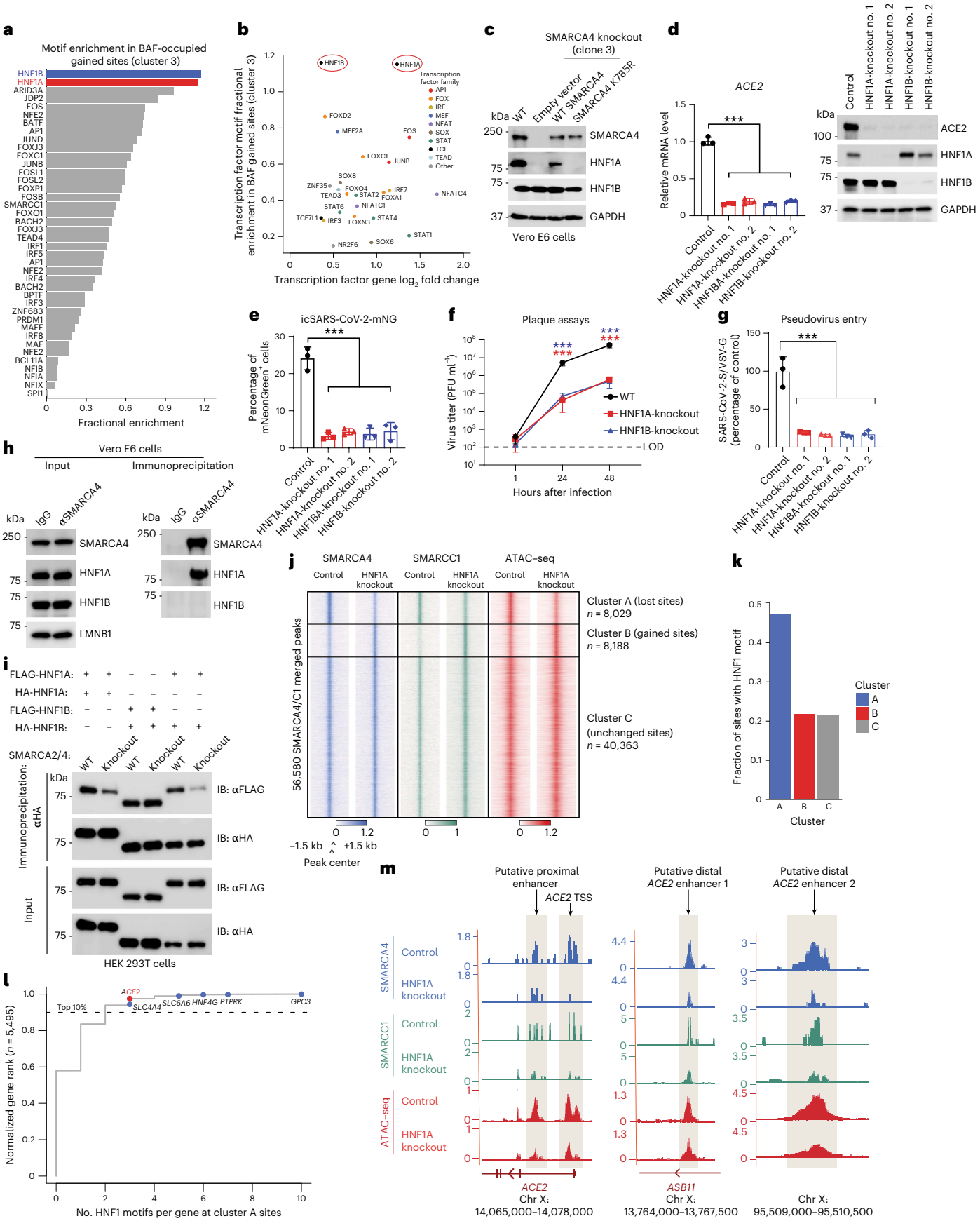

https://doi.org/10.1038/s41588-023-01307-z

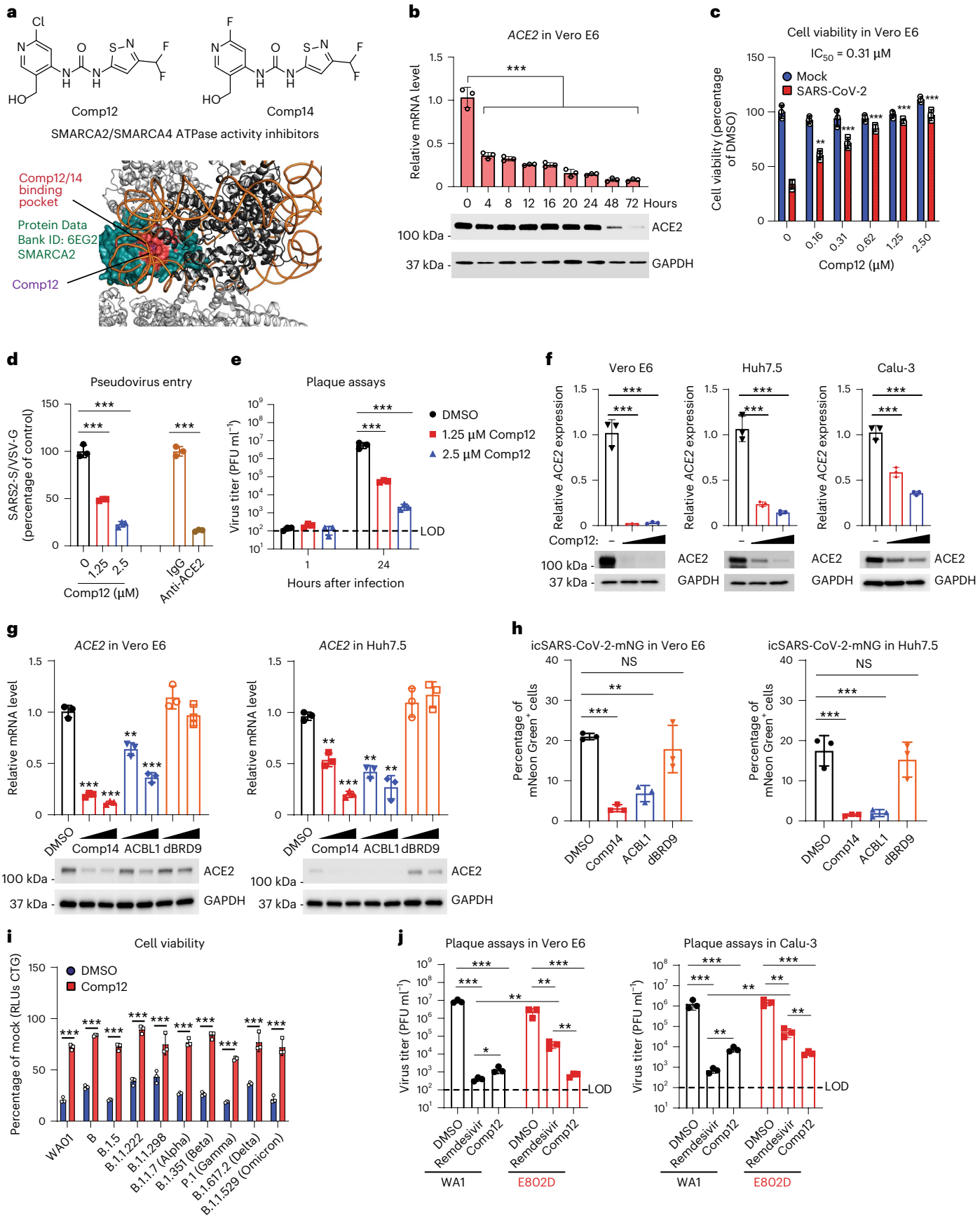

This interaction was dependent on nucleic acids because benzonase treatment abolished binding in the nucleus (Extended Data Fig. 5f,g). Consistent with the overexpression data, immunoprecipitation of endogenous BAF complexes in Vero E6 cells also captured only HNF1A but not HNF1B, despite similar nuclear protein levels (Fig. 3h). Given that both HNF1A and HNF1B motifs were enriched in mSWI/

Fig. 4 | Small-molecule inhibition of the SMARCA4 ATPase of mSWI/SNF complexes downregulates *ACE2* expression and blocks SARS-CoV-2 infection. **a**, Top: chemical structures of the mSWI/SNF SMARCA4/2 ATPase inhibitors, Comp12 and Comp14. Bottom: three-dimensional structure highlighting Comp12 docked in the ATPase site of the SMARCA2/4 ATPase subunit (Protein Data Bank ID: 6EG2). **b**, Vero E6 cells were treated with 1.25 μM Comp12 for the indicated times. ACE2 mRNA and protein levels were measured using RT–qPCR and immunoblot, respectively. **c**, Vero E6 cells were pretreated with Comp12 inhibitors for 2 d and then infected with SARS-CoV-2 at an MOI of 0.2. Cell viability was measured 3 d after infection. **d**, Vero E6 cells were pretreated with 1.25 and 2.5 μM Comp12 for 2 d and then infected with SARS-CoV-2 pseudovirus. The ACE2 antibody was preincubated with cells for 1 h before infection as a positive control. Luciferase relative to VSVpp-VSV-G control was measured 1 d after infection. **e**, SARS-CoV-2 production in Comp12 pretreated Vero E6 cells with the indicated concentrations of Comp12 for 2 d. **f**, *ACE2* transcript and protein levels in Comp12-treated Vero E6, Huh7.5 and Calu-3 cells for 2 d at 1.25 and 2.5 μM. **g**, *ACE2* transcript and protein levels in inhibitor and degrader-treated Vero and Huh7.5 cells for 2 d at 1.25 and 2.5 μM. **h**, Vero E6 and Huh7.5 cells were pretreated with the indicated inhibitors and/or degraders at 2.5 μM for 2 d and then infected with icSARS-CoV-2-mNG. The frequency of infected cells was measured by mNeonGreen expression. **i**, Vero E6 cells were pretreated with 2.5 μM Comp12 for 2 d and then infected with the indicated SARS-CoV-2 variants at an MOI of 0.2. Cell viability was measured 3 d after infection. **j**, Vero E6 or Calu-3 cells were pretreated with 2.5 μM of Comp12 for 2 d and then infected with the SARS-CoV-2 WA1 and E802D viruses. Virus production was measured by plaque assays 1 d after infection. Data in **b**–**j** were analyzed using a one-way ANOVA with Tukey's multiple comparisons test. The mean ± s.e.m. are shown. $^{*}P < 0.05$, $^{**}P < 0.01$, $^{***}P < 0.001$, $n = 3$ biological replicates.

SNF-dependent sites and both HNF1 family transcription factors mediated viral infection, yet only HNF1A was shown to bind BAF complexes, we performed reciprocal immunoprecipitations to determine whether HNF1A/B factors dimerized. Consistent with previous studies, we identified homo- and heterodimers of both HNF1A and HNF1B[52–54]. Further, SMARCA4/2 knockout reduced HNF1A homo- and heterodimerization but did not affect HNF1B homodimerization (Fig. 3i), implicating cBAF as a scaffold for HNF1A function. Taken together, these data highlight the specific tethering of HNF1A to BAF complexes, which can either homo- or heterodimerize in a manner dependent on the physical scaffold of the BAF complex ATPase module SMARCA4/2.

We next performed C&T and ATAC–seq to evaluate changes in genome-wide BAF complex targeting and DNA accessibility, respectively, upon HNF1A knockout. Notably, we identified a cluster of 8,029 sites over which BAF complex occupancy and accessibility was substantially reduced after HNF1A knockout (cluster A, lost sites), along with another cluster of gained sites (cluster B, $n = 8{,}188$) and a large cluster of unchanged sites (cluster C, $n = 40{,}363$, 71% all sites) (Fig. 3j and Extended Data Fig. 5h–j). Importantly, sites losing BAF complex targeting and associated DNA accessibility upon HNF1A knockout exhibited the highest HNF1A motif density (Fig. 3k and Extended Data Fig. 5k). Further, within cluster A (lost sites), the *ACE2* locus scored among the sites of highest HNF1A motif density (Fig. 3l,m and Extended Data Fig. 5l). Taken together, these results highlight the critical role for the HNF1A–BAF complex binding interaction in directing BAF complex localization and remodeling activities to HNF1A target sites genome-wide. These findings underscore the impact of transcription factor DNA motif density in dictating the degree to which BAF complexes localize and act over a given target sequence.

SMARCA4 inhibition blocks *ACE2* expression and viral infection

To investigate the potential of ATPase-competent cBAF complexes as host-directed therapeutic targets for coronavirus disease 2019, we next evaluated the effect of two analogous orally bioavailable small-molecule inhibitors of SMARCA2/4 ATPase activity, Comp12 and Comp14, on SARS-CoV-2 infection[55] (Fig. 4a). Given the role of mSWI/SNF complex ATPase activity in facilitating DNA accessibility over the *ACE2* locus and *ACE2* gene expression, we evaluated the impact of Comp12 treatment on *ACE2* mRNA and protein expression in Vero E6 cells (Fig. 4b). Notably, mRNA levels of *ACE2* were reduced as early as 4 h after treatment with Comp12, while maximal reduction of protein levels required 48–72 h of treatment (Fig. 4b). Further, Comp12 had no effect on *DPP4* expression, which was similar to the SMARCA4 knockout genetic results (Fig. 2h and Extended Data Fig. 6a). Importantly, we observed dose-dependent inhibition of SARS-CoV-2-induced cell death with Comp12 (half maximal inhibitory concentration (IC_{50}) = 310 nM), whereas the cell death induced by MERS-CoV was unaffected (Fig. 4c and Extended Data Fig. 6b). In addition, SMARCA2/4 inhibition with Comp12 reduced SARS-CoV-2 infection and viral entry (Fig. 4d,e) but had no effect on MERS-CoV entry (Extended Data Fig. 6c). We also observed inhibition of *ACE2* expression in Huh7.5 and Calu-3 cells demonstrating that this is generalizable across monkey and human cell lines (Fig. 4f).

Finally, to assess alternate compounds that might block SMARCA4 activity, we tested an analog of Comp12, Comp14 (ref. [55]) and a completely independent PROTAC degrader of SMARCA2/4 and PBRM1 (ACBI1)[56]. As a negative control, we also tested a PROTAC degrader of the ncBAF-specific protein BRD9 (dBRD9)[57]. Both Comp14 and ACBI1 inhibited *ACE2* expression in both Vero E6 and Huh7.5 cells (Fig. 4g), whereas targeting BRD9 had no effect, which is consistent with our genetic results above. Consistent with ACE2 downregulation, Comp14 and ACBI1 treatment inhibited icSARS-CoV-2-mNG replication, virus production and pseudovirus entry (Fig. 4h and Extended Data Fig. 6d,e).

To confirm that the mechanism of ACE2 downregulation identified in Vero E6 cells was consistent in human cell lines, we profiled BAF complex and HNF1A chromatin occupancy (C&T), DNA accessibility (ATAC–seq) and gene expression (RNA sequencing (RNA-seq)) in Huh7.5 and Calu-3 cells treated with dimethyl sulfoxide (DMSO) or Comp12. In both cases, we identified a cluster of sites co-occupied by HNF1A and cBAF (marked by SMARCA4, SMARCC1 and ARID1A) over which occupancy of

Fig. 5 | SMARCA4 is required for *ACE2* expression and sarbecovirus susceptibility in primary human cells. **a**, Schematic of SMARCA4/2 ATPase inhibitor treatment and virus infection in primary HBECs. **b**–**e**, HBECs were pretreated with 2.5 and 5 μM Comp12 for 4 d and then infected with SARS-CoV-2 (**b**), HKU5-SARS1-S (**c**), MERS-CoV (**d**) and IAV (**e**). Virus replication was measured by plaque assay and/or RT–qPCR. **f**, HBECs were pretreated with 2.5 μM Comp12 for 4 d and then infected with SARS-CoV-2 WA1 or E802D virus at an MOI of 0.5. The virus titer was measured using plaque assay. Remdesivir was added right after infection. **g**, *ACE2* expression was measured using RT–qPCR; SARS-CoV-2 replication was measured using a plaque assay after virus infection in HBECs pretreated with 2.5 μM of the indicated compounds for 4 d. **h**, hPSC-derived pneumocyte-like cells were pretreated with Comp12 for 2 d and then infected with SARS-CoV-2 at an MOI of 0.1. **i**,**j**, Infectivity was measured by the accumulation of viral nucleoprotein in the nucleus of the cells 2 d after infection. *ACE2* expression and SARS-CoV-2 infection were measured in HIEs (**i**) and MIEs (**j**) pretreated with 2.5 μM of the indicated compounds for 3 d except remdesivir, which was added right after virus infection. **k**, Model depicting the mechanism of mSWI/SNF complex-mediated regulation of *ACE2* expression and SARS-CoV-2 entry. In **b**, **c**, **d**, **f**, **g** and **i**, the dashed line indicates the limit of detection. Data in **b**–**j** were analyzed using a one-way ANOVA with Tukey's multiple comparisons test. The mean ± s.e.m. are shown. $^{**}P < 0.01$, $^{***}P < 0.001$, $^{****}P < 0.0001$, $n = 3$ biological replicates.

https://doi.org/10.1038/s41588-023-01307-z

both HNF1A and cBAF was lost after treatment with Comp12 (cluster 2) (Extended Data Fig. 7a). These sites also exhibited a corresponding loss in DNA accessibility, were primarily distal in nature and were highly enriched in HNF motifs (Extended Data Fig. 7b–e). Upon ranking cluster 2 sites in both Huh7.5 and Calu-3 cells based on the change in SMARCA4 occupancy in DMSO versus Comp12 conditions, *ACE2* scored

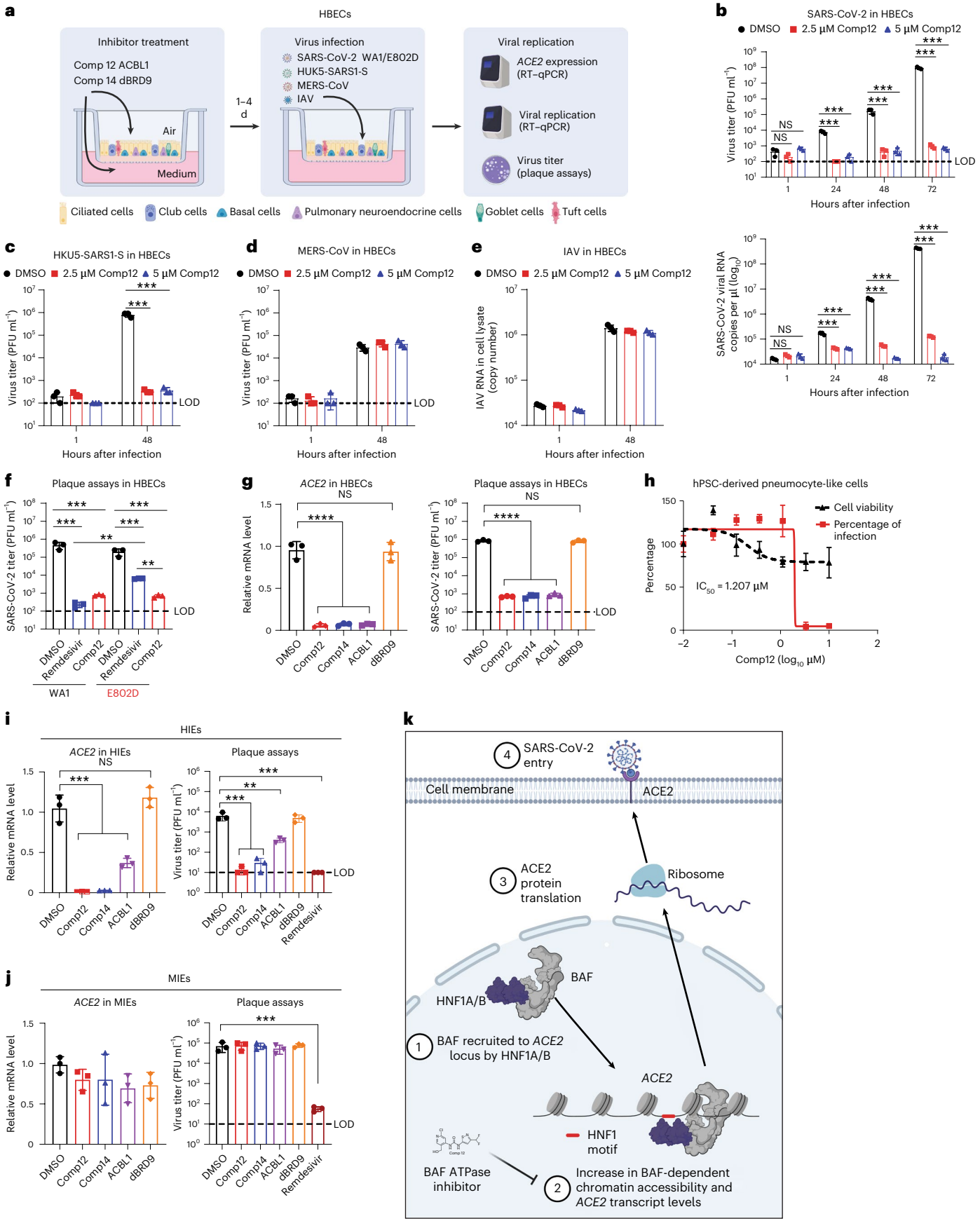

again as a top affected locus (Extended Data Fig. 7f). Transcriptional analysis further identified downregulation of *ACE2* transcript levels in Comp12-treated Huh7.5 and Calu-3 cells, underscoring similar regulation of *ACE2* expression by the cBAF complex and HNF1A across the group of cell lines evaluated (Extended Data Fig. 7g).

We next asked whether mSWI/SNF ATPase inhibition could inhibit diverse SARS-CoV-2 variants and virus resistant to a direct-acting antiviral. Like the antiviral effects observed with the prototypic SARS-CoV-2 WA/01, Comp12 protected cells from infection against nine SARS-CoV-2 variants including: B (Germany); B.1.5 (UK); B.1.1.222 (UK); B.1.1.298 (Denmark); B.1.1.7 (Alpha); B.1.351 (Beta); P.1 (Gamma); B.1.617.2 (Delta); and B.1.1.529 (Omicron) (Fig. 4i). We next determined whether Comp12 can overcome drug-resistant virus infection using a remdesivir-resistant SARS-CoV-2 virus, which contained a point mutation, E802D, in the NSP12 RNA-dependent RNA polymerase[3]. Notably, Comp12 exhibited better efficacy against the E802D mutant virus compared to remdesivir (Fig. 4j). Taken together, these data indicate that inhibition of mSWI/SNF complex ATPase activity is a viable approach to attenuate diverse sarbecoviruses, including SARS-CoV-2 variants of concern and drug-resistant mutants.

BAF inhibition blocks SARS-CoV-2 infection in primary cells

We next sought to evaluate the antiviral effects of mSWI/SNF complex ATPase inhibition in physiologically relevant primary cells. We first evaluated the impact of SMARCA2/4 ATPase inhibition in primary human bronchial epithelial cells (HBECs) cultured at air–liquid interface (ALI) (Fig. 5a). Remarkably, Comp12 treatment nearly completely blocked SARS-CoV-2 viral replication and virus production in HBECs by approximately 5 logs as measured by plaque assay and quantitative PCR (qPCR) (Fig. 5b). Comp12 did not result in cytotoxicity at the concentrations tested in HBECs (Extended Data Fig. 8a). Consistent with our findings across three cell lines, Comp12 downregulated *ACE2* expression in HBECs (Extended Data Fig. 8b). Comp12 pretreatment of HBECs blocked SARS-CoV-2 infection and downregulated both *ACE2* and *HNF1A* (Fig. 5b and Extended Data Fig. 8b,c). Consistently, ACE2 was one of the most highly downregulated genes in HBECs after Comp12 treatment (Extended Data Fig. 8d). Pathway analysis of differentially regulated genes in response to Comp12 treatment did not identify common antiviral pathways, which is consistent with ACE2 downregulation as the main, if not exclusive, mechanism of action (Extended Data Fig. 8e).

To evaluate the antiviral specificity of Comp12, we challenged Comp12-treated HBECs with HKU5-SARS-CoV-1-S, MERS-CoV and influenza A virus (IAV, A/WSN/1933). As expected, Comp12 blocked HKU5-SARS-1-S replication, which also uses the ACE2 receptor, whereas replication of MERS-CoV and IAV, which use DPP4 and sialic acid as receptors, respectively[13,58,59], were unaffected (Fig. 5c–e). We next tested the efficacy of Comp12 in overcoming remdesivir-resistant E802D mutant SARS-CoV-2 infection in HBECs. Comp12 treatment restricted E802D virus replication compared to remdesivir treatment, highlighting the potential usefulness of mSWI/SNF inhibition to combat antiviral drug resistance from currently approved drug classes (Fig. 5f). Consistent with Comp12, Comp14 and ACBI1 treatment downregulated *ACE2* and *HNF1A* expression and restricted SARS-CoV-2 infection (Fig. 5g and Extended Data Fig. 8f). Further, Comp12 treatment also restricted SARS-CoV-2 infection in induced pluripotent stem cell-derived ACE2-expressing cells (Fig. 5h). Taken together, these data demonstrate the tolerability, antiviral efficacy and viral specificity of SMARCA2/4 ATPase inhibition in primary human cells.

Finally, we investigated the therapeutic potential of cBAF ATPase inhibition in vivo in mice (Extended Data Fig. 9a). Surprisingly, Comp14 treatment of WT C57BL/6J mice did not confer protection from mouse-adapted SARS-CoV-2/MA10 as measured by weight loss and virus titers in the lung (Extended Data Fig. 9b–d). We did not observe significant body weight loss in Comp14-treated mice compared to a DMSO control, demonstrating tolerance of mSWI/SNF inhibition (Extended Data Fig. 9b). Consistent with the lack of antiviral efficacy, *Ace2* expression levels in Comp12-treated mice was comparable to that in DMSO-treated mice (Extended Data Fig. 9e). Given this discrepancy between mouse and cell-based human data, we hypothesized that *Ace2* expression in mice is not regulated by the cBAF-HNF1 axis as in humans. To test this hypothesis, we measured the impact of cBAF ATPase inhibition on *ACE2* expression in human and murine intestinal enteroids (MIEs), which endogenously express high levels of ACE2 (ref. [60]). Notably, targeting cBAF ATPase activity downregulated *ACE2* expression and blocked SARS-CoV-2 infection in human intestinal enteroids (HIEs) but not in mouse enteroids (Fig. 5i,j), demonstrating fundamental differences between mouse and human ACE2 regulation. Consistent with this, the density of HNF1 transcription factor binding motifs around the *ACE2* locus was markedly reduced in mice compared to humans (Extended Data Fig. 9f). Collectively, these data suggest that the cBAF complex–HNF1 transcription factor axis specifically regulates ACE2 accessibility and expression in primates (Fig. 5k).

Discussion

In this study, we identified that the transcription factor HNF1A binds to and directs cBAF complexes to the *ACE2* locus. This results in DNA accessibility and induces *ACE2* expression and promotes SARS-CoV-2 susceptibility. This mechanism is conserved across three primate cell lines and three human primary cell types, including airway epithelial cells, and can be therapeutically targeted by orally bioavailable small-molecule inhibitors and degraders of SMARCA4/2 ATPase subunits. mSWI/SNF complex disruption, by either genetic or small-molecule means, potently reduces *ACE2* expression and sarbecovirus infection in cell lines and primary human airway epithelial cells by up to 5 logs, underscoring the potential prophylactic and therapeutic activity of mSWI/SNF inhibitors for current and emerging pandemic sarbecoviruses.

Viral receptor expression is a major determinant of pathogenesis[61–64]. Understanding the molecular mechanisms of the regulation and dynamics of *ACE2* expression may inform host range, tissue and cell type susceptibility, as well as disease severity. Recent studies have revealed that *ACE2* expression increases with age[65], smoking[66], infection[67] and interferons[67–69]; however, the molecular mechanisms governing the dynamic regulation of *ACE2* gene expression are incompletely understood. The detrimental phenotypes associated with *Ace2* germline disruption in mice are attributed to the increase in angiotensin II resulting from *Ace2* deficiency. The effects and tolerability of transient ablation of ACE2, such as that resulting from SMARCA4 inhibition, in adult animals is unclear[70–73].

Several genome-wide CRISPR–Cas9 screens in the context of SARS-CoV-2 have been now described[22–25,74–77]. SMARCA4 was identified as the second highest hit next to ACE2 in our screen[22] and was also enriched in a recent screen[23]. SMARCA4 and other mSWI/SNF complex genes were not identified in several other screens, probably owing to the fact that these cell lines ectopically overexpressed ACE2 (that is, in A549 cells and Huh7.5 cells), thus decoupling *ACE2* expression from the endogenous gene regulatory elements needed for mSWI/SNF action, as we show also in this study (Fig. 2i)[24,76,77]. Further, in two screens performed at 37 °C with Huh7.5 cells expressing only endogenous ACE2, ACE2 itself was not detected as a statistically significant hit[25,74]; similarly, in a screen performed at 33 °C with Huh7.5 cells, ACE2 ranked only at 171 out of 19,364 genes[25]. These discrepancies highlight the challenges in detecting genes important for ACE2 regulation in Huh7.5 genome-wide screens and may be due to the limited virus-induced cell death in this cell context. Importantly, we validated the importance of SMARCA4-mediated catalytic activity of mSWI/SNF complexes in Vero E6, Huh7.5, Calu-3 and primary HBEC cells, human induced pluripotent stem cells and HIEs and identified the mechanism by which it regulates *ACE2* expression, reconciling these screening-based discrepancies in the field.

We identified a mechanistic axis by which mSWI/SNF complexes remodel the *ACE2* and *HNF1A* loci, generating DNA accessibility and activating gene expression. HNF1A protein, production of which is dependent on ATPase-active mSWI/SNF complexes, binds mSWI/SNF complexes, guiding complex targeting on the genome to sites of high HNF1A/B motif density, including the *ACE2* locus. Further, our finding that HNF1A but not HNF1B binds BAF complexes, and that homo- and heterodimerization of HNF1 factors requires SMARCA4 and hence fully formed BAF complexes containing the ATPase module[29,34], suggests a role for BAF complex chromatin binding and nucleosome remodeling for the dimerization of transcription factors such as HNF1A/B. These data will require additional biochemical and structural studies to further define the nature of dimeric transcription factor–BAF complex interactions. Interestingly, HNF1A/B transcription factors exhibit substantial functional differences between mice and humans, with HNF1 transcription factor motifs depleted at the mouse *Ace2* locus relative to the primate *ACE2* locus[78]. Consistent with this, we did not observe *Ace2* downregulation or antiviral activity of SMARCA4 inhibitors in mouse enteroids or in vivo in mice. This highlights a limitation of rodent models for assessing *Ace2* expression and drugs modulating mSWI/SNF complexes or *Ace2*.

New therapeutics are needed for current and emerging coronaviruses to increase antiviral breadth, combat emerging drug resistance and improve tolerability. Currently, host-directed therapeutics predominantly focus on modulating pathogenic immune activation, such as with the steroid dexamethasone[79,80]. In this study, we describe the SMARCA4/2 ATPase, which is specific to mSWI/SNF complexes, as a host-directed therapeutic target independent of immune modulation. SMARCA2/4 ATPase antagonists are currently in phase I clinical trials for SMARCA2/4-dependent cancers, such as uveal melanoma and acute myeloid leukemia (NCT04879017 and NCT04891757) highlighting the feasibility of this approach. Targeting mSWI/SNF complexes in a transient manner offers several potential advantages in the regulation of *ACE2* expression and sarbecovirus infection. First, given the mechanism of mSWI/SNF complexes in regulating genomic accessibility in the host cell, viral antagonism is anticipated to be synergistic with existing, direct-acting antiviral and host immunomodulatory drugs. Second, by downregulating ACE2, SMARCA4 inhibitors can inhibit diverse ACE2-utilizing viruses including HCoV-NL63, SARS-CoV-1, SARS-CoV-2 variants, including remdesivir-resistant forms, and sarbecoviruses recently discovered in bats, which represent a substantial risk for causing future pandemics in humans[81–85]. Taken together, our data suggest that comprehensive studies in humans to evaluate the safety and efficacy of small-molecule antagonists of SMARCA4-mediated mSWI/SNF ATPase activity are warranted and may provide prophylactic and therapeutic benefit for pandemic coronaviruses.

Online content

Any methods, additional references, Nature Portfolio reporting summaries, source data, extended data, supplementary information, acknowledgements, peer review information; details of author contributions and competing interests; and statements of data and code availability are available at https://doi.org/10.1038/s41588-023-01307-z.

References

1. Bergwerk, M. et al. Covid-19 breakthrough infections in vaccinated health care workers. *N. Engl. J. Med.* **385**, 1474–1484 (2021).
2. V'Kovski, P., Kratzel, A., Steiner, S., Stalder, H. & Thiel, V. Coronavirus biology and replication: implications for SARS-CoV-2. *Nat. Rev. Microbiol.* **19**, 155–170 (2021).
3. Gandhi, S. et al. De novo emergence of a remdesivir resistance mutation during treatment of persistent SARS-CoV-2 infection in an immunocompromised patient: a case report. *Nat. Commun.* **13**, 1547 (2022).
4. Heilmann, E. et al. SARS-CoV-2 3CL^{pro} mutations selected in a VSV-based system confer resistance to nirmatrelvir, ensitrelvir, and GC376. *Sci. Transl. Med.* **15**, eabq7360 (2023).
5. Hu, Y. et al. Naturally occurring mutations of SARS-CoV-2 main protease confer drug resistance to nirmatrelvir. Preprint at *bioRxiv* https://doi.org/10.1101/2022.06.28.497978 (2022).
6. Stevens, L. J. et al. Mutations in the SARS-CoV-2 RNA dependent RNA polymerase confer resistance to remdesivir by distinct mechanisms. *Sci. Transl. Med.* **14**, eabo0718 (2022).
7. Zhou, Y. et al. Nirmatrelvir-resistant SARS-CoV-2 variants with high fitness in an infectious cell culture system. *Sci. Adv.* **8**, eadd7197 (2022).
8. Zumla, A., Hui, D. S., Azhar, E. I., Memish, Z. A. & Maeurer, M. Reducing mortality from 2019-nCoV: host-directed therapies should be an option. *Lancet* **395**, e35–e36 (2020).
9. Krause, P. R. et al. SARS-CoV-2 variants and vaccines. *N. Engl. J. Med.* **385**, 179–186 (2021).
10. Meganck, R. M. & Baric, R. S. Developing therapeutic approaches for twenty-first-century emerging infectious viral diseases. *Nat. Med.* **27**, 401–410 (2021).
11. Li, W. et al. Angiotensin-converting enzyme 2 is a functional receptor for the SARS coronavirus. *Nature* **426**, 450–454 (2003).
12. Hofmann, H. et al. Human coronavirus NL63 employs the severe acute respiratory syndrome coronavirus receptor for cellular entry. *Proc. Natl Acad. Sci. USA* **102**, 7988–7993 (2005).
13. Raj, V. S. et al. Dipeptidyl peptidase 4 is a functional receptor for the emerging human coronavirus-EMC. *Nature* **495**, 251–254 (2013).
14. Hoffmann, M. et al. SARS-CoV-2 cell entry depends on ACE2 and TMPRSS2 and is blocked by a clinically proven protease inhibitor. *Cell* **181**, 271–280 (2020).
15. Walls, A. C. et al. Structure, function, and antigenicity of the SARS-CoV-2 spike glycoprotein. *Cell* **181**, 281–292 (2020).
16. Yan, R. et al. Structural basis for the recognition of SARS-CoV-2 by full-length human ACE2. *Science* **367**, 1444–1448 (2020).
17. Zang, R. et al. TMPRSS2 and TMPRSS4 promote SARS-CoV-2 infection of human small intestinal enterocytes. *Sci. Immunol.* **5**, eabc3582 (2020).
18. Hoffmann, M., Kleine-Weber, H. & Pöhlmann, S. A multibasic cleavage site in the spike protein of SARS-CoV-2 is essential for infection of human lung cells. *Mol. Cell* **78**, 779–784 (2020).
19. Snijder, E. J. et al. Unique and conserved features of genome and proteome of SARS-coronavirus, an early split-off from the coronavirus group 2 lineage. *J. Mol. Biol.* **331**, 991–1004 (2003).
20. Stertz, S. et al. The intracellular sites of early replication and budding of SARS-coronavirus. *Virology* **361**, 304–315 (2007).
21. Knoops, K. et al. SARS-coronavirus replication is supported by a reticulovesicular network of modified endoplasmic reticulum. *PLoS Biol.* **6**, e226 (2008).
22. Wei, J. et al. Genome-wide CRISPR screens reveal host factors critical for SARS-CoV-2 infection. *Cell* **184**, 76–91 (2021).
23. Rebendenne, A. et al. Bidirectional genome-wide CRISPR screens reveal host factors regulating SARS-CoV-2, MERS-CoV and seasonal HCoVs. *Nat. Genet.* **54**, 1090–1102 (2022).
24. Daniloski, Z. et al. Identification of required host factors for SARS-CoV-2 infection in human cells. *Cell* **184**, 92–105 (2021).
25. Schneider, W. M. et al. Genome-scale identification of SARS-CoV-2 and pan-coronavirus host factor networks. *Cell* **184**, 120–132 (2021).
26. Kadoch, C. & Crabtree, G. R. Mammalian SWI/SNF chromatin remodeling complexes and cancer: mechanistic insights gained from human genomics. *Sci. Adv.* **1**, e1500447 (2015).
27. Kadoch, C. et al. Proteomic and bioinformatic analysis of mammalian SWI/SNF complexes identifies extensive roles in human malignancy. *Nat. Genet.* **45**, 592–601 (2013).

28. Clapier, C. R. & Cairns, B. R. The biology of chromatin remodeling complexes. *Annu. Rev. Biochem.* **78**, 273–304 (2009).
29. Mashtalir, N. et al. Modular organization and assembly of SWI/SNF family chromatin remodeling complexes. *Cell* **175**, 1272–1288 (2018).
30. Michel, B. C. et al. A non-canonical SWI/SNF complex is a synthetic lethal target in cancers driven by BAF complex perturbation. *Nat. Cell Biol.* **20**, 1410–1420 (2018).
31. Mashtalir, N. et al. Chromatin landscape signals differentially dictate the activities of mSWI/SNF family complexes. *Science* **373**, 306–315 (2021).
32. Khavari, P. A., Peterson, C. L., Tamkun, J. W., Mendel, D. B. & Crabtree, G. R. BRG1 contains a conserved domain of the SWI2/SNF2 family necessary for normal mitotic growth and transcription. *Nature* **366**, 170–174 (1993).
33. Mashtalir, N. et al. A structural model of the endogenous human BAF complex informs disease mechanisms. *Cell* **183**, 802–817 (2020).
34. Pan, J. et al. The ATPase module of mammalian SWI/SNF family complexes mediates subcomplex identity and catalytic activity-independent genomic targeting. *Nat. Genet.* **51**, 618–626 (2019).
35. Valencia, A. M. et al. Recurrent SMARCB1 mutations reveal a nucleosome acidic patch interaction site that potentiates mSWI/SNF complex chromatin remodeling. *Cell* **179**, 1342–1356 (2019).
36. Nakayama, R. T. et al. SMARCB1 is required for widespread BAF complex-mediated activation of enhancers and bivalent promoters. *Nat. Genet.* **49**, 1613–1623 (2017).
37. Kelso, T. W. R. et al. Chromatin accessibility underlies synthetic lethality of SWI/SNF subunits in ARID1A-mutant cancers. *eLife* **6**, e30506 (2017).
38. Wang, X. et al. SMARCB1-mediated SWI/SNF complex function is essential for enhancer regulation. *Nat. Genet.* **49**, 289–295 (2017).
39. Valencia, A. M. & Kadoch, C. Chromatin regulatory mechanisms and therapeutic opportunities in cancer. *Nat. Cell Biol.* **21**, 152–161 (2019).
40. Versteege, I. et al. Truncating mutations of hSNF5/INI1 in aggressive paediatric cancer. *Nature* **394**, 203–206 (1998).
41. Santen, G. W. E., Kriek, M. & van Attikum, H. SWI/SNF complex in disorder: SWItching from malignancies to intellectual disability. *Epigenetics* **7**, 1219–1224 (2012).
42. Pan, J. et al. Interrogation of mammalian protein complex structure, function, and membership using genome-scale fitness screens. *Cell Syst.* **6**, 555–568 (2018).
43. Xie, X. et al. An infectious cDNA clone of SARS-CoV-2. *Cell Host Microbe* **27**, 841–848 (2020).
44. Bultman, S. J., Gebuhr, T. C. & Magnuson, T. A Brg1 mutation that uncouples ATPase activity from chromatin remodeling reveals an essential role for SWI/SNF-related complexes in β-globin expression and erythroid development. *Genes Dev.* **19**, 2849–2861 (2005).
45. Hodges, H. C. et al. Dominant-negative SMARCA4 mutants alter the accessibility landscape of tissue-unrestricted enhancers. *Nat. Struct. Mol. Biol.* **25**, 61–72 (2018).
46. Bultman, S. et al. A *Brg1* null mutation in the mouse reveals functional differences among mammalian SWI/SNF complexes. *Mol. Cell* **6**, 1287–1295 (2000).
47. Hota, S. K. & Bruneau, B. G. ATP-dependent chromatin remodeling during mammalian development. *Development* **143**, 2882–2897 (2016).
48. Santen, G. W. E. et al. Coffin–Siris syndrome and the BAF complex: genotype–phenotype study in 63 patients. *Hum. Mutat.* **34**, 1519–1528 (2013).
49. Kaya-Okur, H. S. et al. CUT&Tag for efficient epigenomic profiling of small samples and single cells. *Nat. Commun.* **10**, 1930 (2019).
50. Corces, M. R. et al. An improved ATAC–seq protocol reduces background and enables interrogation of frozen tissues. *Nat. Methods* **14**, 959–962 (2017).
51. Buenrostro, J. D., Giresi, P. G., Zaba, L. C., Chang, H. Y. & Greenleaf, W. J. Transposition of native chromatin for fast and sensitive epigenomic profiling of open chromatin, DNA-binding proteins and nucleosome position. *Nat. Methods* **10**, 1213–1218 (2013).
52. Tomei, L., Cortese, R. & De Francesco, R. A POU-A related region dictates DNA binding specificity of LFB1/HNF1 by orienting the two XL-homeodomains in the dimer. *EMBO J.* **11**, 4119–4129 (1992).
53. Mendel, D. B. et al. Characterization of a cofactor that regulates dimerization of a mammalian homeodomain protein. *Science* **254**, 1762–1767 (1991).
54. Mendel, D. B., Hansen, L. P., Graves, M. K., Conley, P. B. & Crabtree, G. R. HNF-1α and HNF-1β (vHNF-1) share dimerization and homeo domains, but not activation domains, and form heterodimers in vitro. *Genes Dev.* **5**, 1042–1056 (1991).
55. Papillon, J. P. N. et al. Discovery of orally active inhibitors of Brahma homolog (BRM)/SMARCA2 ATPase activity for the treatment of Brahma related gene 1 (BRG1)/SMARCA4-mutant cancers. *J. Med. Chem.* **61**, 10155–10172 (2018).
56. Farnaby, W. et al. BAF complex vulnerabilities in cancer demonstrated via structure-based PROTAC design. *Nat. Chem. Biol.* **15**, 672–680 (2019).
57. Remillard, D. et al. Degradation of the BAF complex factor BRD9 by heterobifunctional ligands. *Angew. Chem. Int. Ed. Engl.* **56**, 5738–5743 (2017).
58. Schauer, R. Sialic acids as regulators of molecular and cellular interactions. *Curr. Opin. Struct. Biol.* **19**, 507–514 (2009).
59. Gottschalk, A. On the mechanism underlying initiation of influenza virus infection. *Ergeb. Mikrobiol. Immunitatsforsch Exp. Ther.* **32**, 1–22 (1959).
60. Zhou, J. et al. Infection of bat and human intestinal organoids by SARS-CoV-2. *Nat. Med.* **26**, 1077–1083 (2020).
61. Wilen, C. B. et al. Tropism for tuft cells determines immune promotion of norovirus pathogenesis. *Science* **360**, 204–208 (2018).
62. Orchard, R. C. et al. Discovery of a proteinaceous cellular receptor for a norovirus. *Science* **353**, 933–936 (2016).
63. Marsh, M. & Helenius, A. Virus entry: open sesame. *Cell* **124**, 729–740 (2006).
64. Grove, J. & Marsh, M. The cell biology of receptor-mediated virus entry. *J. Cell Biol.* **195**, 1071–1082 (2011).
65. Chow, R. D., Majety, M. & Chen, S. The aging transcriptome and cellular landscape of the human lung in relation to SARS-CoV-2. *Nat. Commun.* **12**, 4 (2021).
66. Almeida-da-Silva, C. L. C., Matshik Dakafay, H. & Liu, K. Cigarette smoke stimulates SARS-CoV-2 internalization by activating AhR and increasing ACE2 expression in human gingival epithelial cells. *Int. J. Mol. Sci.* **22**, 7669 (2021).
67. Onabajo, O. O. et al. Interferons and viruses induce a novel truncated ACE2 isoform and not the full-length SARS-CoV-2 receptor. *Nat. Genet.* **52**, 1283–1293 (2020).
68. Lee, H. K., Jung, O. & Hennighausen, L. JAK inhibitors dampen activation of interferon-stimulated transcription of ACE2 isoforms in human airway epithelial cells. *Commun. Biol.* **4**, 654 (2021).
69. Jankowski, J., Lee, H. K., Wilflingseder, J. & Hennighausen, L. JAK inhibitors dampen activation of interferon-activated transcriptomes and the SARS-CoV-2 receptor ACE2 in human renal proximal tubules. *iScience* **24**, 102928 (2021).
70. Curfman, G. Renin-angiotensin-aldosterone inhibitors and susceptibility to and severity of COVID-19. *JAMA* **324**, 177–178 (2020).

71. Mancia, G., Rea, F., Ludergnani, M., Apolone, G. & Corrao, G. Renin–angiotensin–aldosterone system blockers and the risk of Covid-19. *N. Engl. J. Med.* **382**, 2431–2440 (2020).
72. Reynolds, H. R. et al. Renin–angiotensin–aldosterone system inhibitors and risk of Covid-19. *N. Engl. J. Med.* **382**, 2441–2448 (2020).
73. Wysocki, J., Lores, E., Ye, M., Soler, M. J. & Batlle, D. Kidney and lung ACE2 expression after an ACE inhibitor or an Ang II receptor blocker: implications for COVID-19. *J. Am. Soc. Nephrol.* **31**, 1941–1943 (2020).
74. Baggen, J. et al. Genome-wide CRISPR screening identifies TMEM106B as a proviral host factor for SARS-CoV-2. *Nat. Genet.* **53**, 435–444 (2021).
75. Biering, S. B. et al. Genome-wide bidirectional CRISPR screens identify mucins as host factors modulating SARS-CoV-2 infection. *Nat. Genet.* **54**, 1078–1089 (2022).
76. Wang, R. et al. Genetic screens identify host factors for SARS-CoV-2 and common cold coronaviruses. *Cell* **184**, 106–119 (2021).
77. Zhu, Y. et al. A genome-wide CRISPR screen identifies host factors that regulate SARS-CoV-2 entry. *Nat. Commun.* **12**, 961 (2021).
78. Harries, L. W., Brown, J. E. & Gloyn, A. L. Species-specific differences in the expression of the *HNF1A*, *HNF1B* and *HNF4A* genes. *PLoS ONE* **4**, e7855 (2009).
79. Ledford, H. Coronavirus breakthrough: dexamethasone is first drug shown to save lives. *Nature* **582**, 469 (2020).
80. Ho, J. S. Y. et al. TOP1 inhibition therapy protects against SARS-CoV-2-induced lethal inflammation. *Cell* **184**, 2618–2632(2021).
81. Zhou, H. et al. Identification of novel bat coronaviruses sheds light on the evolutionary origins of SARS-CoV-2 and related viruses. *Cell* **184**, 4380–4391 (2021).
82. Ge, X.-Y. et al. Isolation and characterization of a bat SARS-like coronavirus that uses the ACE2 receptor. *Nature* **503**, 535–538 (2013).
83. Li, H. et al. Human–animal interactions and bat coronavirus spillover potential among rural residents in Southern China. *Biosaf. Health* **1**, 84–90 (2019).
84. Menachery, V. D. et al. SARS-like WIV1-CoV poised for human emergence. *Proc. Natl Acad. Sci. USA* **113**, 3048–3053 (2016).
85. Wang, N. et al. Serological evidence of bat SARS-related coronavirus infection in humans, China. *Virol. Sin.* **33**, 104–107 (2018).

[1]Department of Laboratory Medicine, Yale School of Medicine, New Haven, CT, USA. [2]Department of Immunobiology, Yale School of Medicine, New Haven, CT, USA. [3]Department of Pediatric Oncology, Dana-Farber Cancer Institute and Harvard Medical School, Boston, MA, USA. [4]Broad Institute of MIT and Harvard, Cambridge, MA, USA. [5]Program in Virology, Harvard Medical School, Boston, MA, USA. [6]Department of Cancer Biology, Dana-Farber Cancer Institute, Boston, MA, USA. [7]Department of Medicine, Harvard Medical School, Boston, MA, USA. [8]Hillman Cancer Center, University of Pittsburgh Medical Center, Pittsburgh, PA, USA. [9]Genetic Perturbation Platform, Broad Institute of MIT and Harvard, Cambridge, MA, USA. [10]Department of Microbiology, Icahn School of Medicine at Mount Sinai, New York, NY, USA. [11]Global Health Emerging Pathogens Institute, Icahn School of Medicine at Mount Sinai, New York, NY, USA. [12]Division of Infectious Diseases, Department of Medicine, Icahn School of Medicine at Mount Sinai, New York, NY, USA. [13]Tisch Cancer Institute, Icahn School of Medicine at Mount Sinai, New York, NY, USA. [14]Department of Pathology, Molecular and Cell based Medicine, Icahn School of Medicine at Mount Sinai, New York, NY, USA. [15]Huffington Center for Cell-based Research in Parkinson's Disease, Icahn School of Medicine at Mount Sinai, New York, NY, USA. [16]Department of Cell, Developmental and Regenerative Biology, Icahn School of Medicine at Mount Sinai, New York, NY, USA. [17]Black Family Stem Cell Institute, Icahn School of Medicine at Mount Sinai, New York, NY, USA. [18]Department of Pathology, Yale School of Medicine, New Haven, CT, USA. [19]Yale Cancer Center, Yale School of Medicine, New Haven, CT, USA. [20]Howard Hughes Medical Institute, Chevy Chase, MD, USA. [21]These authors contributed equally: Jin Wei, Ajinkya Patil. [22]These authors jointly supervised this work: Cigall Kadoch, Craig B. Wilen. ✉e-mail: cigall_kadoch@dfci.harvard.edu; craig.wilen@yale.edu

Methods

Blinding statement

Data collection and analysis were not performed blind to the conditions of the experiments.

Data exclusion statement

No animals or data were excluded from the analyses in this study.

Cells

HEK 293T (cat. no. CRL-3216, ATCC), Vero E6 (cat. no. CRL-1586, ATCC) and Huh7.5 (Washington University in St. Louis) cells were cultured in DMEM with 10% heat-inactivated FCS and 1% penicillin-streptomycin unless otherwise indicated. Calu-3 (cat. no. HTB-55, ATCC) cells were cultured in RPMI 1640 medium with GlutaMAX, 10% FCS, 1% penicillin-streptomycin and 16 ng ml^{-1} of hepatocyte growth factor (Stem Cell Technology) to preserve viability and support robust growth. For Vero E6 and Huh7.5 cells, 5 µg ml^{-1} of puromycin (Gibco) and 5 µg ml^{-1} blasticidin (Gibco) were added as appropriate. For Calu-3 cells, 1 µg ml^{-1} of puromycin was added as appropriate.

ALI culture of HBECs and infection

Primary HBECs were purchased from Lonza (cat. no. CC-2541) and differentiated in ALI culture as described previously[86]. HBECs were cultured in suspension in PneumaCult-Ex Plus Medium according to the manufacturer's instructions (STEMCELL Technologies). To generate the ALI cultures, HBECs were plated on collagen-coated transwell inserts with a 0.4-µ pore size (Corning) at 5×10^4 cells per ml per filter and inserted into 24-well culture plates. Cells were maintained for the first 3 d in PneumaCult-Ex Plus Medium then changed to PneumaCult-ALI Medium (STEMCELL Technologies) containing the ROCK inhibitor Y-27632 for 4 d. Fresh medium, 100 µl in the apical chamber and 500 µl in the basal chamber, was provided every day. On day 7, the medium at the apical chambers was removed, while the basal chambers were maintained with 500 µl of PneumaCult-ALI Medium. Medium in the basal chamber was changed every 2–3 d. HBECs were maintained at ALI culture for 28 d, allowing them to differentiate.

Differentiated HBECs were pretreated with inhibitors or DMSO for 1–4 d at both apical and basal sides. HBECs were washed five times with PBS and inoculated with SARS-CoV-2, HKU5-SARS-CoV-1-S, MERS-CoV and IAV from the apical side at a multiplicity of infection (MOI) of 0.5; the cell number per filter support was approximately 5×10^5. After 1 h of incubation at 37 °C, HBECs were rinsed with PBS twice to remove unbound viral particles. Infected HBECs were further maintained under ALI conditions at 37 °C in 5% CO_2. At different time points, 100 µl of fresh medium was added to the apical surface and the cultures were incubated for 30 min at 37 °C. The supernatants were collected at different times after virus infection and the viruses were titrated by plaque assays on Vero E6 cells. The cell lysates were collected in TRIzol for qPCR analysis.

HIE and MIE culture and infection

HIEs (J2) derived from a biopsy specimen were kindly provided by M. Estes from Baylor College of Medicine through the Texas Medical Center Digestive Diseases Center Enteroid Core. Protocols for the culture, maintenance and differentiation of HIEs were based on previous studies[87,88]. Briefly, frozen vials of HIEs were thawed out and resuspended in Cultrex Reduced Growth Factor Basement Membrane Extract (BME) (equivalent of Matrigel), Type 2, Select (R&D Systems). The BME mixture (25 µl per well) was plated as droplets onto 24-well tissue culture plates and polymerized at 37 °C for 10 min. Then, 500 µl of growth medium was added to each well and changed every other day. After approximately 7–10 d, HIEs were expanded from 1 well to 3 wells. For HIEs differentiation, growth medium was replaced with an equal volume of differentiation medium and incubated for 4–5 d with medium being changed every other day until use.

MIEs were derived from the ileal tissue of C57BL/6J mice that were approximately 6 weeks old. MIEs were derived by collecting the distal ileal tissue aseptically under the hood. The intestine was flushed and washed with PBS and opened longitudinally to further remove intestinal contents. With sterile scissors, ileal tissues kept on ice in a dish were minced until pieces were small enough to be pipetted with a P1000. Then, 1 ml of collagenase solution (100 mg collagenase type I and 0.001% v/v gentamicin mixed in washing medium) was added to the minced tissue and incubated at 37 °C for 20 min and pipetted every 5 min. The tissue mixture was filtered through a 40-µm strainer and then washed with 9 ml washing medium (DMEM/F12, 100× L-glutamine, 100× penicillin-streptomycin, 10% FCS). Filtrate mixture (containing the crypts) was transferred into a 15-ml falcon tube and were pelleted at 400 *g* for 5 min. Pelleted crypts were suspended into 25 µl BME per well and plated onto 24-well plates. Then, 500 µl of growth medium (50% conditioned medium L-WRN)[88] was added to each well. After approximately 5 d, MIEs were expanded from 1 well to 3–4 wells. For MIE differentiation, growth medium was replaced with the same volume of differentiation medium and incubated for approximately 4 d with medium changed every other day before use.

Differentiated HIEs and MIE cells were pretreated with the indicated small molecules or DMSO for 3 d in three-dimensional organoid culture. HIEs and MIEs were infected with SARS-CoV-2 at 10^5 PFU ml^{-1}. After 1 h of incubation at 37 °C, the medium was replaced with fresh medium. The cells with medium were frozen and thawed. The supernatants were collected and the viruses were titrated by plaque assays on Vero E6 cells.

H9 stem cell-derived pneumocyte-like cell differentiation and SARS-CoV-2 infection

Human pluripotent stem cells (hPSC cells) (H9) (obtained from WiCell) were grown with mTeSR (cat. no. 85850, STEMCELL Technologies) on Vitronectin XF-coated (cat. no. 07180, STEMCELL Technologies) tissue culture plates and divided using Gentle Cell Dissociation Reagent every 5–6 d (cat. no. 07174, STEMCELL Technologies). Alveolar differentiation was produced as described previously[89]. On day 9 after differentiation induction, the biosafety level 3 (BSL-3) facility performed viral infections in accordance with Icahn School of Medicine at Mount Sinai (ISMMS)-developed biosafety protocols. Two days before infection, the medium was replaced with 100 µl of medium containing the compound of interest at concentrations 50% greater than those indicated, including a DMSO control. Plates were then transferred into the BSL-3 facility and 4,000 PFU (MOI = 0.1) of SARS-CoV-2/WA1 was added in 50 µl of medium, bringing the final compound concentrations to those indicated. Plates were then incubated for 48 h at 37 °C. After infection, supernatants were removed and cells were fixed with 4% formaldehyde for 24 h before being removed from the BSL-3 facility. Cells were then immunostained for the viral nucleoprotein (an in-house monoclonal antibody 1C7, provided by T. Moran) with a DAPI counterstain. Infected (488 nM) and total cells (DAPI) were quantified using the Celigo (Nexcelom Bioscience) imaging cytometer. Infectivity was measured by the accumulation of viral nucleoprotein in the nucleus of the cells (fluorescence accumulation). Percentage infection was quantified as ((infected cells/total cells) − background) × 100 and the DMSO control was then set to 100% infection for analysis. The IC_{50} and IC_{90} for each experiment were determined using Prism 8 (GraphPad Software). Cytotoxicity was measured using the MTT assay (Roche) according to the manufacturer's instructions. In uninfected cells, cytotoxicity was measured with same compound dilutions and concurrently with the viral replication assay. All assays were performed in biologically independent triplicates.

Expression constructs and lentiviral infection

All constructs were PCR-amplified from complementary DNA (cDNA) using Q5 High-Fidelity DNA Polymerase with GC buffer (New England

Biolabs). For HA- or FLAG-tag HNF1A and HNF1B, the purified fragments were cloned into a lenti-cytomegalovirus vector containing puromycin resistance. pLX307-WT SMARCA4 and its K785R mutant were as described previously[34]. All constructs were sequence-validated. For lentiviral transduction, cells were transduced at 50% confluency and selected with puromycin 48 h later.

Viral stocks

To generate viral stocks (Supplementary Table 1) Vero E6 or Vero E6-ACE2-TMPRSS2 cells were inoculated with HKU5-SARS-CoV-1-S (NR-48814), SARS-CoV-2 isolate USA-WA1/2020 (NR-52281), Germany isolate B (NR-52370), B.1.5 (NR-53944), B.1.222 (NR-53945), B.1.1.298 (NR-53953), B.1.1.7 (NR-54000), B.1.351 (NR-54008), P.1 (NR-54982), B.1.617.2 (NR-55611) and MERS-CoV (NR-48813) from BEI resources. B.1.1.529 was isolated from a patient at Yale New Haven Hospital[90] (icSARS-CoV-2-mNG (provided by the World Reference Center for Emerging Viruses and Arboviruses))[43] at an MOI of approximately 0.01 for 3 d to generate a P1 stock. The P1 stock was then used to inoculate Vero E6 or Vero E6-ACE2-TMPRSS2 cells for 1–3 d at approximately 50% cytopathic effects. Supernatant was collected and clarified by centrifugation (450 *g* × 5 min) and filtered through a 0.45-µm filter and then aliquoted for storage at −80 °C. Virus titer was determined by plaque assay using Vero E6 cells. All work with infectious virus was performed in a BSL-3 laboratory and approved by the Yale University Biosafety Committee.

SARS-CoV-2 plaque assays

Vero E6 or Vero E6-ACE2-TMPRSS2 cells were seeded at 4×10^5 cells per well onto 12-well plates. The following day, the medium was removed and replaced with 100 µl of tenfold serial dilutions of virus. Plates were incubated at 37 °C for 1 h with gentle rocking. Subsequently, overlay medium (DMEM, 2% FCS, 0.6% Avicel RC-581) was added to each well. At 2 d after infection, plates were fixed with 10% formaldehyde for 30 min, stained with crystal violet solution (0.5% crystal violet in 20% ethanol) for 30 min and then rinsed with deionized water to visualize plaques.

SARS-CoV-2 fluorescence-based reporter virus assay

Cells were plated at 2.5×10^3 cells per well onto a 384-well plate and incubated at 37 °C overnight. Cells were infected with icSARS-CoV-2-mNG at an MOI of 1. The frequencies of infected cells were measured by mNeonGreen expression and were assessed 2 d after infection using high-content imaging (Cytation 5, Agilent Technologies). Infection frequencies were calculated as the ratio between mNeonGreen$^+$ cells and total cells in bright-field[22].

Generation of polyclonal knockout cell lines

Oligonucleotides corresponding to the target sequences were synthesized by Yale Keck Oligo facility (Supplementary Table 2). Double-stranded oligonucleotides were cloned into the lentiCRISPR-V2 vector and cotransfected packaging plasmids into 293T cells. Lentiviral particles were collected and used to transduce Vero E6, Huh7.5 or Calu-3 cells. Infected cells were selected with puromycin for 2 weeks before additional experiments were performed.

To isolate a clonal Vero E6 or Huh7.5 HNF1A and HNF1B knockout cell lines, polyclonal HNF1A and HNF1B knockout cells were diluted and plated onto 96-well plates. Single colonies were grown and clones were screened for HNF1A or HNF1B knockout by western blot.

Generation of SMARCA4 knockout and complemented cells

Vero E6 SMARCA4 knockout cells were generated by lipofection of Cas9 ribonucleoproteins (RNPs). CRISPR guide RNA (gRNA) were synthesized by Integrated DNA Technologies (Supplementary Table 2). gRNAs were complexed at a 1:1 molar ratio with ATTO550-labeled trans-activating CRISPR RNA (tracrRNA) in TE buffer by heating at 95 °C for 5 min followed by cooling to room temperature to form crRNA–tracrRNA duplexes. Alt-R Cas9 enzyme was combined with the crRNA–tracrRNA duplex at room temperature for 20 min to form RNP complexes in Opti-MEM with 50 µl total volume. Complexes were mixed with Lipofectamine RNAiMAX for 10 min at room temperature before transfection was performed. Single cells were then sorted by flow cytometry and SMARCA4 knockout was confirmed by western blot. SMARCA4 knockout clones were complemented by lentiviral transduction of pLX307 vector or containing full-length SMARCA4 or ATPase-dead mutant K785R with a C-terminal V5 tag. Two days after transduction, puromycin was added and cells were selected for 5 d. The expression of SMARCA4 in complemented cells was detected by western blot.

SMARCA2/4 inhibitor treatment for cell lines

ACBI1 was purchased from MedChemExpress (cat. no. HY-128359); Comp12 and Comp14 were synthesized as described previously[55]. Vero E6 cells (1.5×10^4) were pretreated with the indicated concentration of Comp12 for 48 h and then infected with SARS-CoV-2 or MERS-CoV at an MOI of 0.2. Cell viability was quantified by CTG 3 d after infection. Vero E6, Huh7.5 and Calu-3 cells (1×10^6) were pretreated with 2.5 µM Comp12 for 48 h, then *ACE2* expression was detected by quantitative PCR with reverse transcription (RT–qPCR) and western blot. Cytotoxicity was not observed in these cell lines during the time and at the concentration of drug used.

Pseudovirus production

Vesicular stomatitis virus (VSV)-based pseudotype viruses were produced as described previously[22,91]. Briefly, 293T cells were transfected with pCAGGS or pcDNA3.1 vector expressing the CoV S glycoprotein and then inoculated with a replication-deficient VSV virus that contained the expression cassettes for *Renilla* luciferase instead of the VSV-G open reading frame. After an incubation period of 1 h at 37 °C, the inoculum was removed and cells were washed with PBS before medium supplemented with anti-VSV-G clone I4 was added to neutralize residual input virus (no antibody was added to cells expressing VSV-G). Pseudotyped particles were collected 24 h after inoculation, clarified from cellular debris by centrifugation and stored at −80 °C before use.

Pseudovirus entry assay

A total of 1×10^4 Vero E6, Huh7.5 or Calu-3 cells were seeded in 100 µl total volume in each well of a black-walled clear bottom 96-well plate. The following day pseudovirus was added at a 1:10 final concentration v/v and incubated for 1 d. Cells were lysed with *Renilla* Luciferase Assay System (Promega Corporation) according to the manufacturer's instructions. Luciferase activity was measured using a microplate reader (Synergy or Cytation 5, BioTek Instruments).

Small-molecule inhibitor treatment and SARS-CoV-2 (MA10) infection in mice

C57BL/6J mice were injected intraperitoneally daily with Comp14 (25 mg kg^{-1}) for 1–4 d or Comp12 (10 mg kg^{-1}) for 5 d. For the Comp12 treatment, tissues (lung, liver, heart and small intestine) were collected and homogenized in 1 ml of DMEM supplemented with 2% heat-inactivated FCS and 1% penicillin-streptomycin. Then, 250 µl of homogenate was mixed with 750 µl of TRIzol LS (Invitrogen) and RNA was extracted with Direct-zol RNA MiniPrep Plus Kit (Zymo Research) for *ACE2* expression. For infections, mice were anesthetized with 30% v/v isoflurane diluted in propylene glycol (30% isoflurane) and administered mouse-adapted SARS-CoV-2 MA10 intranasally in 50 µl of PBS. At 2 d after infection, the left lobe of the lung was collected and homogenized in 1 ml of DMEM supplemented with 2% heat-inactivated FCS and 1% penicillin-streptomycin. Lung homogenates were clarified by centrifugation at 3,200 *g* for 10 min and stored in aliquots at −80 °C. Viral burden was measured in lung homogenates by plaque assay on Vero E6 cells. In addition, 250 µl of lung homogenate was mixed with

750 µl of TRIzol LS and RNA was extracted with the Direct-zol RNA MiniPrep Plus Kit according to the manufacturer's instructions. Mice of both sexes aged between 8 and 10 weeks old were used for this study. All work with SARS-CoV-2 (MA10) was performed in a BSL-3 facility with approval from Environmental Health and Safety and the Institutional Animal Care and Use Committee at Yale University. Mice were randomized based on sex for these experiments.

RT–qPCR

Total RNA was isolated from cells using the Direct-zol RNA MiniPrep Plus Kit and 1 µg RNA was used for cDNA synthesis. qPCR was carried out using specific primers outlined in Supplementary Table 3.

Coimmunoprecipitation

Cells were lysed in 1 ml NP-40 lysis buffer (cat. no. J60766, Alfa Aesar). For each immunoprecipitation, 0.5–2 µg of the indicated antibody or control IgG and 30 µl of Protein G Sepharose (GoldBio) were incubated with 0.5 ml lysate for at least 3 h. The Sepharose beads were washed three times with lysis buffer containing 500 mM NaCl. The precipitates were analyzed by western blot.

Western blot

Cells were collected and lysed in NP-40 lysis buffer. The cell lysates or coimmunoprecipitates were fractionated on SDS–polyacrylamide gel electrophoresis and transferred to a polyvinylidene fluoride membrane. Immunoblotting analyses were performed with the indicated antibodies and visualized either with horseradish peroxidase-coupled goat anti-mouse/rabbit IgG using a chemiluminescence detection system (ChemiDoc MP, BioRad Laboratories) or by IR680/IR800-conjugated anti-rabbit/mouse antibodies (imaged using an Odyssey CLx imaging system, LI-COR Biosciences).

RNA-seq

Cellular RNA (2×10^6 cells) was extracted in two biological replicates using the Direct-zol RNA MiniPrep Kit. RNA from Vero E6 cells was submitted to the Yale Center for Genome Analysis for library preparation and sequenced on a NovaSeq 6000 instrument. Huh7.5, Calu-3 and HBEC RNA libraries were prepared using the NEBNext Ultra II RNA Library Prep Kit for Illumina (New England Biolabs) and sequenced on a NextSeq 500 instrument.

ATAC–seq

The omni-ATAC protocol was used to probe DNA accessibility with slight modifications covered below[50]. A total of 100,000 cells per sample were trypsinized and washed with cold PBS to remove trypsin. Cell pellets were lysed in 50 µl cold resuspension buffer (RSB) supplemented with fresh NP-40 (final 0.1% v/v), Tween-20 (final 0.1% v/v), digitonin (final 0.01% v/v) (RSB recipe: 10 mM Tris-HCl, pH 7.4, 10 mM NaCl and 3 mM $MgCl_2$). The lysis step was quenched with 1 ml of RSB supplemented with Tween-20 (final 0.1% v/v) and nuclei were pelleted at 500 *g* for 10 min at 4 °C after incubating on ice for 3 min. Nuclei were resuspended in 50 µl transposition reaction mix containing 25 µl 2× Tagmentation DNA Buffer (Illumina), 2.5 µl Tn5 transposase (Illumina), 16.5 µl 1× PBS, 0.5 µl 1% digitonin (final 0.01% v/v), 0.5 µl 10% Tween-20 (final 0.1% v/v) and 5 µl nuclease-free water. The transposition reaction was incubated at 37 °C for 30 min with constant shaking (1,000 r.p.m.) on a thermomixer. Tagmented DNA was purified using the QIAGEN minElute Reaction Cleanup Kit. A standard ATAC–seq amplification protocol with seven cycles of amplification was used to amplify tagmented libraries[92]. Libraries were sequenced on a NextSeq 500 (Illumina) using 37-bp paired-end sequencing.

C&T

C&T was carried out using a protocol developed by Epicypher (www.epicypher.com/content/documents/protocols/cutana-cut&tag-protocol.pdf) in 8-strip PCR tubes with slight modifications as described below. Briefly, concanavalin A-coated (ConA) magnetic beads were activated with Bead Activation Buffer containing 20 mM HEPES, pH 7.9, 10 mM KCl, 1 mM $CaCl_2$, 1 mM $MnCl_2$; beads were stored on ice until used. A total of 300,000 cells per sample were trypsinized and pelleted by centrifugation at room temperature (600 *g* for 3 min). Cells were lysed using cold Nuclear Extraction Buffer containing 20 mM HEPES-KOH, pH 7.9, 10 mM KCl, 0.1% Triton X-100, 20% glycerol supplemented with fresh 0.5 mM spermidine and cOmplete, Mini, EDTA-free protease inhibitor (Roche) for 2 min. Nuclei were pelleted by centrifugation (600 *g* for 3 min), resuspended in 100 µl per sample RSB (20 mM HEPES-KOH, pH 7.9, 150 mM NaCl supplemented with fresh 0.5 mM spermidine and cOmplete, Mini, EDTA-free protease inhibitor) and incubated with activated ConA beads at room temperature for 15 min. The nucleus–ConA bead complex was resuspended in Antibody 150 Buffer containing 20 mM HEPES, pH 7.5, 150 mM NaCl, supplemented with fresh 0.5 mM spermidine, protease inhibitor, 0.01% digitonin and 0.5 µg primary antibody per sample. After overnight incubation at 4 °C on a nutator, supernatant was discarded and beads were washed once with Digitonin 150 Buffer containing 20 mM HEPES, pH 7.5, 150 mM NaCl, supplemented with fresh 0.5 mM spermidine, protease inhibitor, and 0.01% digitonin. The ConA–nuclei complexes were then incubated with Digitonin 150 Buffer supplemented with 0.5 µg per sample secondary antibody for 1 h at room temperature on a nutator. They were then washed with Digitonin 150 Buffer twice before resuspension in 50 µl cold Digitonin 300 Buffer containing 20 mM HEPES, pH 7.5, 300 mM NaCl, supplemented with fresh 0.5 mM spermidine, protease inhibitor and 0.01% digitonin. Then, 2.0 µl CUTANA pAG-Tn5 (Epicypher) was added to each sample and incubated on a nutator for 1 h at room temperature. After incubation, beads were washed twice with cold Digitonin 300 Buffer. Targeted chromatin tagmentation and library amplification were carried out according to the Epicypher's protocol cited above. Libraries were sequenced on a NextSeq 500 instrument using 37-bp paired-end sequencing.

Antibodies

All primary and secondary antibodies used in this study are listed in Supplementary Table 4.

Next-generation sequencing data processing

C&T, ATAC–seq and human RNA-seq samples were sequenced with the Illumina NextSeq 500 platform; RNA-seq samples from Vero E6 cells were sequenced with the Illumina NovaSeq 6000 platform. For the RNA-seq data, reads were aligned to either the chlSab2 (NCBI annotation release 100) or the hg19 reference genome using STAR aligner v2.7.3a[93] with the parameters --winAnchorMultimapNmax 200--outFilterMultimapNmax 100--quantMode GeneCounts. bigWig files were generated using the deepTools v.3.1.3 bamCoverage function[94] with the normalizeUsingRPKM option. Output gene count tables from STAR were used as input into the edgeR v.3.12.1 R software package[95] to evaluate differential gene expression. For the ATAC–seq data, read trimming was carried out using Trimmomatic v.0.36 (ref. [96]) followed by alignment, duplicate read removal and read quality filtering using Bowtie2 (ref. [97]), Picard v.2.8.0 (http://broadinstitute.github.io/picard/) and SAMtools v.0.1.19 (ref. [98]), respectively. ATAC–seq peaks were called with MACS2 v.2.1 (ref. [99]) using the BAMPE option and a broad peak cutoff of 0.001. For ATAC–seq track generation, output BAM files were converted into bigWig files using the MACS2 and UCSC utilities[100] to display coverage throughout the genome in reads per million (RPM) values. For the C&T libraries, the CutRunTools pipeline was leveraged to perform read trimming, quality filtering, alignment, peak calling and track building using default parameters[101]. All sequencing data analyzed in this study have been deposited at the NCBI's Gene Expression Omnibus (GEO) under accession no. GSE186201.

C&T and ATAC–seq data analyses

Heatmaps and metaplots displaying signals aligned to peak centers were generated using ngsplot v.2.63 (ref. [102]). RPM values were quantile-normalized across samples and *k*-means clustering was applied to partition the data into groups. The bedtools multiIntersectBed and merge functions were used for peak merging[103]; distance-to-TSS peak distributions were computed using Ensembl gene coordinates provided by the UCSC genome browser. Principle component analysis was performed using the wt.scale and fast.svd functions from the corpcor R package on C&T quantile-normalized $\log_2$-transformed RPKM values within merged peaks[104,105]. Transcription factor motif positions within peaks were identified using the MEME FIMO v.4.12.0 software[106] with position frequency matrices curated previously[107]; motif fractions of occurrence within clusters of peaks were computed using in-house scripts.

Quantification and statistical analysis

All statistical analyses were performed in Prism 8 unless otherwise stated. The error bars represent the s.e.m. Viral shedding over time was analyzed by repeated-measures analysis of variance (ANOVA). All statistically analyzed pairwise comparisons are indicated with a bar and the *P* value is represented by $^{*}P < 0.05$, $^{**}P < 0.01$, $^{***}P < 0.0001$ and $^{****}P < 0.00001$. The absence of a bar indicates that no statistical pairwise comparisons were made. *P* values are listed in Supplementary Table 5.

Ethics statement

This research complies with all relevant ethical regulations and the research protocols are approved by the Yale School of Medicine, Dana-Farber Cancer Institute and ISMMS. All animal work was approved by the Institutional Animal Care and Use Committee at Yale University School of Medicine according to its guidelines. All infection work was performed in an animal BSL-3 facility at Yale University School of Medicine.

Reporting summary

Further information on research design is available in the Nature Portfolio Reporting Summary linked to this article.

Data availability

The RNA-seq, CUT&Tag and ATAC–seq data generated during this study are available at GEO under accession no. GSE186201. Source data are provided with this paper.

Code availability

No custom code was generated for this study.

References

86. Ravindra, N. G. et al. Single-cell longitudinal analysis of SARS-CoV-2 infection in human airway epithelium identifies target cells, alterations in gene expression, and cell state changes. *PLoS Biol.* **19**, e3001143 (2021).
87. Ettayebi, K. et al. Replication of human noroviruses in stem cell-derived human enteroids. *Science* **353**, 1387–1393 (2016).
88. Co, J. Y. et al. Controlling epithelial polarity: a human enteroid model for host–pathogen interactions. *Cell Rep.* **26**, 2509–2520 (2019).
89. Riva, L. et al. Discovery of SARS-CoV-2 antiviral drugs through large-scale compound repurposing. *Nature* **586**, 113–119 (2020).
90. Pérez-Then, E. et al. Neutralizing antibodies against the SARS-CoV-2 Delta and Omicron variants following heterologous CoronaVac plus BNT162b2 booster vaccination. *Nat. Med.* **28**, 481–485 (2022).
91. Avanzato, V. A. et al. A structural basis for antibody-mediated neutralization of Nipah virus reveals a site of vulnerability at the fusion glycoprotein apex. *Proc. Natl Acad. Sci. USA* **116**, 25057–25067 (2019).
92. Buenrostro, J. D., Wu, B., Chang, H. Y. & Greenleaf, W. J. ATAC–seq: a method for assaying chromatin accessibility genome-wide. *Curr. Protoc. Mol. Biol.* **109**, 21.29.1–21.29.9 (2015).
93. Dobin, A. et al. STAR: ultrafast universal RNA-seq aligner. *Bioinformatics* **29**, 15–21 (2013).
94. Ramírez, F. et al. deepTools2: a next generation web server for deep-sequencing data analysis. *Nucleic Acids Res.* **44**, W160–W165 (2016).
95. Robinson, M. D., McCarthy, D. J. & Smyth, G. K. edgeR: a Bioconductor package for differential expression analysis of digital gene expression data. *Bioinformatics* **26**, 139–140 (2010).
96. Bolger, A. M., Lohse, M. & Usadel, B. Trimmomatic: a flexible trimmer for Illumina sequence data. *Bioinformatics* **30**, 2114–2120 (2014).
97. Langmead, B. & Salzberg, S. L. Fast gapped-read alignment with Bowtie 2. *Nat. Methods* **9**, 357–359 (2012).
98. Li, H. et al. The Sequence Alignment/Map format and SAMtools. *Bioinformatics* **25**, 2078–2079 (2009).
99. Zhang, Y. et al. Model-based analysis of ChIP–Seq (MACS). *Genome Biol.* **9**, R137 (2008).
100. Kuhn, R. M., Haussler, D. & Kent, W. J. The UCSC genome browser and associated tools. *Brief. Bioinformatics* **14**, 144–161 (2013).
101. Zhu, Q., Liu, N., Orkin, S. H. & Yuan, G.-C. CUT&RUNTools: a flexible pipeline for CUT&RUN processing and footprint analysis. *Genome Biol.* **20**, 192 (2019).
102. Shen, L., Shao, N., Liu, X. & Nestler, E. ngs.plot: quick mining and visualization of next-generation sequencing data by integrating genomic databases. *BMC Genomics* **15**, 284 (2014).
103. Quinlan, A. R. & Hall, I. M. BEDTools: a flexible suite of utilities for comparing genomic features. *Bioinformatics* **26**, 841–842 (2010).
104. Schäfer, J. & Strimmer, K. A shrinkage approach to large-scale covariance matrix estimation and implications for functional genomics. *Stat. Appl. Genet. Mol. Biol.* https://doi.org/10.2202/1544-6115.1175 (2005).
105. Opgen-Rhein, R. & Strimmer, K. Accurate ranking of differentially expressed genes by a distribution-free shrinkage approach. *Stat. Appl. Genet. Mol. Biol.* https://doi.org/10.2202/1544-6115.1252 (2007).
106. Grant, C. E., Bailey, T. L. & Noble, W. S. FIMO: scanning for occurrences of a given motif. *Bioinformatics* **27**, 1017–1018 (2011).
107. Grossman, S. R. et al. Positional specificity of different transcription factor classes within enhancers. *Proc. Natl Acad. Sci. USA* **115**, E7222–E7230 (2018).

Acknowledgements

We thank members of the Wilen and Kadoch laboratories for helpful discussions and feedback throughout the course of this project. We also thank the World Reference Center for Emerging Viruses and Arboviruses and BEI resources for critical reagents; M. Simon for helpful discussions; M. Feeley, Y. Lee, the Yale Center for Genome Analysis and Yale Center for Molecular Discovery for technical assistance; B. Fontes for environmental health and safety; and Z. Herbert and M. Berkeley of the Dana-Farber Cancer Institute Molecular Biology Core Facility for help with sequencing studies. Figure 5a,k and Extended Data Figs. 1a and 9a were created with BioRender. Work at the K.M.W. and A.G.-S. laboratory on this study was funded by the Center for Research on Influenza Pathogenesis and Transmission, a National Institute of Allergy and Infectious Diseases (NIAID)-funded Center of Excellence for influenza Research and Response (contract no. 75N93021C00014), and from NIAID grant no. U19AI135972, Department of Defense grant no. W81XWH-20-1-0270 and Defense

Advanced Research Projects Agency grant no. HR0011-19-2-319 0020. This work was supported by a National Institutes of Health (NIH) grant no. K08 AI128043 (C.B.W.), the Burroughs Wellcome Fund (C.B.W.), the Smith Family Foundation (C.B.W.), the Ludwig Family Foundation (C.B.W.), the Huffington Foundation (Y.Q. and T.P.Z.), the Mathers Foundation (C.B.W.), an Emergent Ventures Fast Grant (C.B.W.), the Mark Foundation for Cancer Research Emerging Leader Award 18-032-ELA (C.K.) and the NIH Director's New Innovator Award no. 1DP2CA195762-01 (C.K.).

Author contributions

J.W., A.P., M.M.A., J.Q., C.K. and C.B.W. conceptualized the study. J.W., A.P., C.K.C., M.M.A., J.G.D., C.K. and C.B.W. devised the methodology. J.W., A.P., M.M.A., M.S.S., B.L. Menasche, R.B.F., A.O., M.A.P.-H., J.K., Y.L., A.M., R.R., B.L. McGovern, M.L.R., A.G.-S., K.M.W., Y.Q. and C.B.W. carried out the investigation. J.W., A.P., M.M.A. and M.S.S. validated the study. J.W., A.P., C.K.C., M.M.A., W.L.C., P.C.D., R.E.H., Q.Y., J.Q., C.K. and C.B.W. carried out the formal data analysis. J.W., A.P., W.L.C. and C.K.C. visualized the data. T.P.Z., J.G.D., A.I., J.Q., C.K. and C.B.W. provided the resources. J.W., A.P., C.K.C., W.L.C., B.L. Menasche, P.C.D. and R.E.H. curated the data. J.W., A.P., C.K. and C.B.W. wrote the paper. C.K. and C.B.W. supervised the study. C.B.W. and C.K. acquired the funding.

Competing interests

C.K. is the scientific founder, scientific advisor to the board of directors, scientific advisory board member, shareholder and consultant for Foghorn Therapeutics. C.K. also serves on the scientific advisory boards of Nereid Therapeutics, Nested Therapeutics and Fibrogen, and is a consultant for Cell Signaling Technology and Google Ventures. J.W., A.P., C.K. and C.B.W. have a patent pending related to this work. C.B.W. is a consultant for Exscientia and Bain Capital Life Sciences and sits on the scientific advisory board for ExcepGen. The A.G.-S. laboratory has received research support from Pfizer, Senhwa Biosciences, Kenall Manufacturing, Avimex, Johnson & Johnson, Dynavax, 7Hills Pharma, Pharmamar, ImmunityBio, Accurius, Nanocomposix, Hexamer, N-FOLD LLC, Model Medicines, Atea Pharma, Applied Biological Laboratories and Merck, outside of the reported work. A.G.-S. has consulting agreements for the following companies involving cash and/or stock: Vivaldi Biosciences; Contrafect; 7Hills Pharma; Avimex; Vaxalto; Pagoda; Accurius; Esperovax; Farmak; Applied Biological Laboratories; Pharmamar; Paratus; CureLab Oncology; CureLab Veterinary; Synairgen and Pfizer, outside of the reported work. A.G.-S. has been an invited speaker in meeting events organized by Seqirus, Janssen, Abbott and AstraZeneca. A.G.-S. is the inventor on patents and patent applications on the use of antivirals and vaccines for the treatment and prevention of virus infections and cancer, owned by the ISMMS, outside of the reported work. J.G.D. consults for Microsoft Research, Abata Therapeutics, Maze Therapeutics, BioNTech, Sangamo and Pfizer. J.G.D. consults for and has equity in Tango Therapeutics. J.G.D. serves as a paid scientific advisor to the Laboratory for Genomics Research, funded in part by GSK, and the Innovative Genomics Institute, funded in part by Apple Tree Partners. J.G.D. receives funding support from the Functional Genomics Consortium: Abbvie, Bristol Myers Squibb, Janssen, Merck and Vir Biotechnology. J.G.D.'s interests are reviewed and managed by the Broad Institute in accordance with its conflict of interest policies. T.P.Z. is an inventor on patents and patent applications on the use of iPS cells and viruses, owned by the Icahn School of Medicine at Mount Sinai, New York. T.P.Z. is a founder and shareholder of Paratus Sciences. The other authors declare no competing interests.

Additional information

Extended data is available for this paper at https://doi.org/10.1038/s41588-023-01307-z.

Supplementary information The online version contains supplementary material available at https://doi.org/10.1038/s41588-023-01307-z.

Correspondence and requests for materials should be addressed to Cigall Kadoch or Craig B. Wilen.

Peer review information *Nature Genetics* thanks the anonymous reviewers for their contribution to the peer review of this work.

https://doi.org/10.1038/s41588-023-01307-z

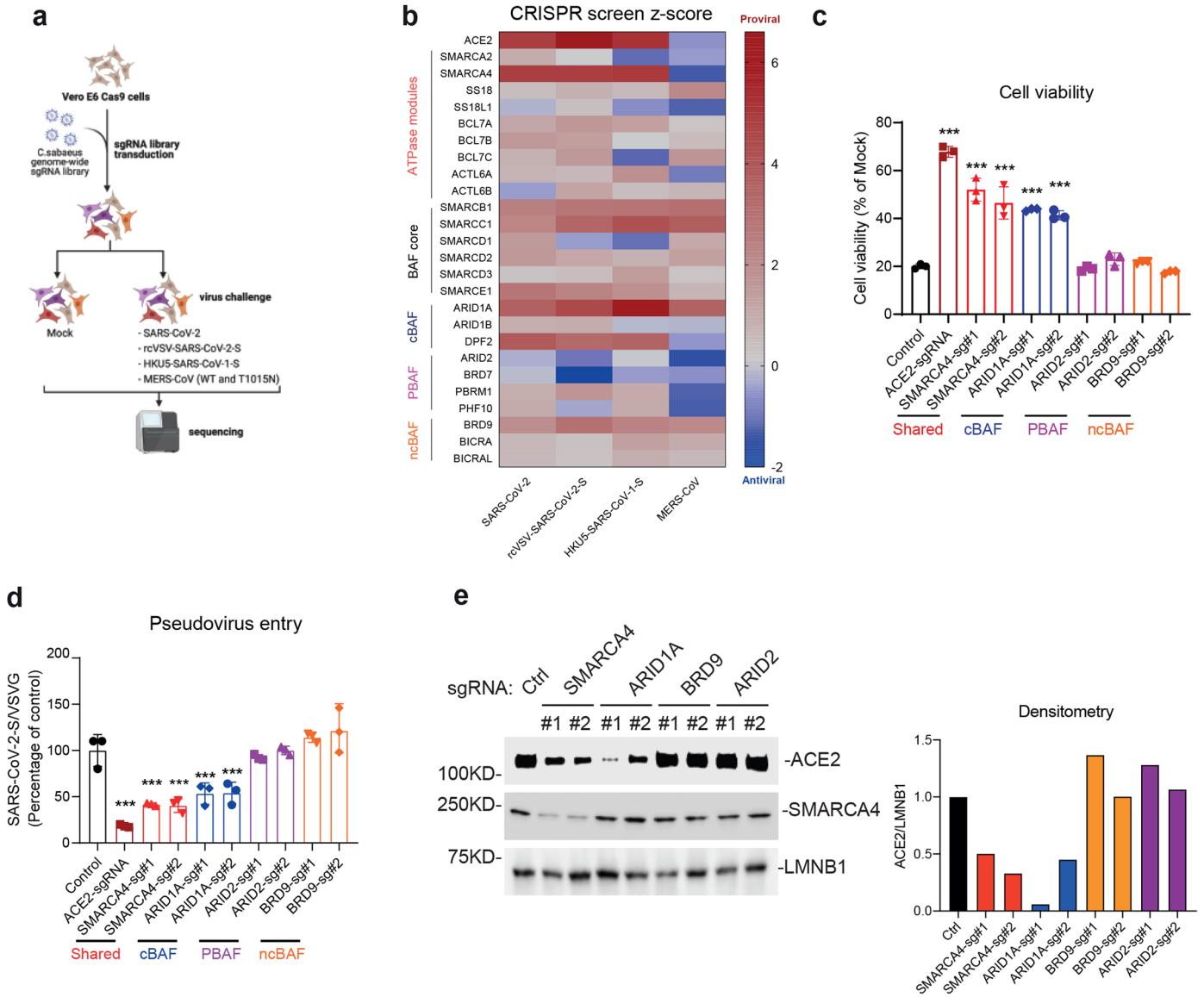

Extended Data Fig. 1 | Canonical BAF (cBAF) is essential for SARS-CoV-2 infection at viral entry in Vero E6 cells. **(a)** Schematic of CRISPR/Cas9-based screen to identify SARS-CoV-2 anti- and pro-viral determinants. **(b)** Heatmap of z-scores of mSWI/SNF complex subunits (cBAF, PBAF, ncBAF) in SARS-CoV-2, rcVSV-SARS-CoV-2-S, HKU5-SARS-CoV-1-S, and MERS-CoV CRISPR resistance screens. **(c)** Polyclonal KO of BAF complex subunits and ACE2 KO cells were infected with SARS-CoV-2 at an MOI of 0.2. Cell viability relative to an uninfected control was measured 3 dpi with CellTiter Glo. **(d)** Vero E6 cells were infected with VSV pseudovirus (VSVpp): VSVpp-VSV-G and VSVpp-SARS-CoV-2-S. Luciferase relative to a VSVpp-VSV-G control was measured 1 dpi. **(e)** Left, CRISPR-mediated SMARCA4 knockout was confirmed by Western blot in Vero E6 cells; Right, densitometry analysis of ACE2 levels normalized to LMNB1. Data in (c-d) were analyzed by one-way ANOVA with Tukey's multiple comparison test. Shown are mean ± SEM. *p < 0.05, **p < 0.01, ***p < 0.001, n = 3 biological replicates. Data in (e) is one representative one of three independent experiments.

https://doi.org/10.1038/s41588-023-01307-z

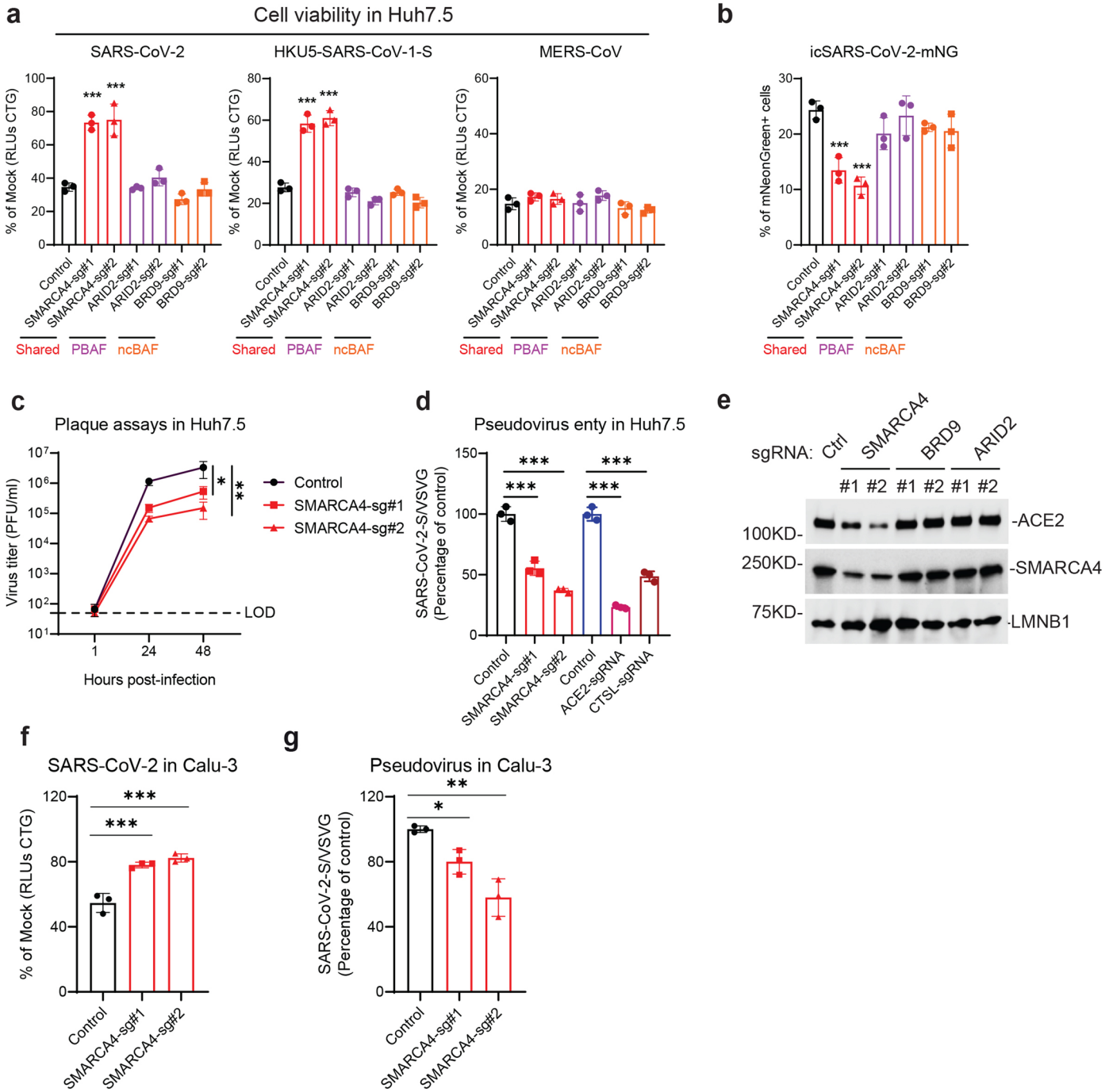

Extended Data Fig. 2 | cBAF is essential for SARS-CoV-2 viral entry in human cells. (a) BAF complex subunit polyclonal KO pools of Huh7.5 cells were infected with SARS-CoV-2, HKU5-SARS-CoV-1-S and MERS-CoV at an MOI of 0.2. Cell viability relative to an uninfected control was measured 4 dpi using CellTiter Glo. **(b)** Bar graph depicting % mNeonGreen-expressing cells (control cells or those with polyclonal CRISPR-mediated KO of shared or unique mSWI/SNF subunits) following infection by icSARS-CoV-2-mNG at an MOI of 1. **(c)** Huh7.5 cells were infected with SARS-CoV-2 at an MOI of 0.1. Virus titer was measured by plaque assay. Dash line, limit of detection. **(d)** Cells were infected with VSV pseudovirus (VSVpp): VSVpp-VSV-G and VSVpp-SARS-CoV-2-S. Luciferase relative to a VSVpp-VSV-G control was measured 1 dpi. **(e)** CRISPR-mediated SMARCA4 knockout was confirmed by Western blot in Huh7.5 cells. **(f)** Calu-3 cells were infected with SARS-CoV-2 at an MOI of 0.2. Cell viability relative to an uninfected control was measured 3 dpi with CellTiter Glo. **(g)** Calu-3 cells were infected with VSV pseudovirus (VSVpp): VSVpp-VSV-G and VSVpp-SARS-CoV-2-S. Luciferase relative to a VSVpp-VSV-G control was measured 1 dpi. Data in (a-d, f-g) were analyzed by one-way ANOVA with Tukey's multiple comparison test. Shown are mean ± SEM. *p < 0.05, **p < 0.01, ***p < 0.001. n = 3 biological replicates. Data in (e) is one representative one of three independent experiments.

https://doi.org/10.1038/s41588-023-01307-z

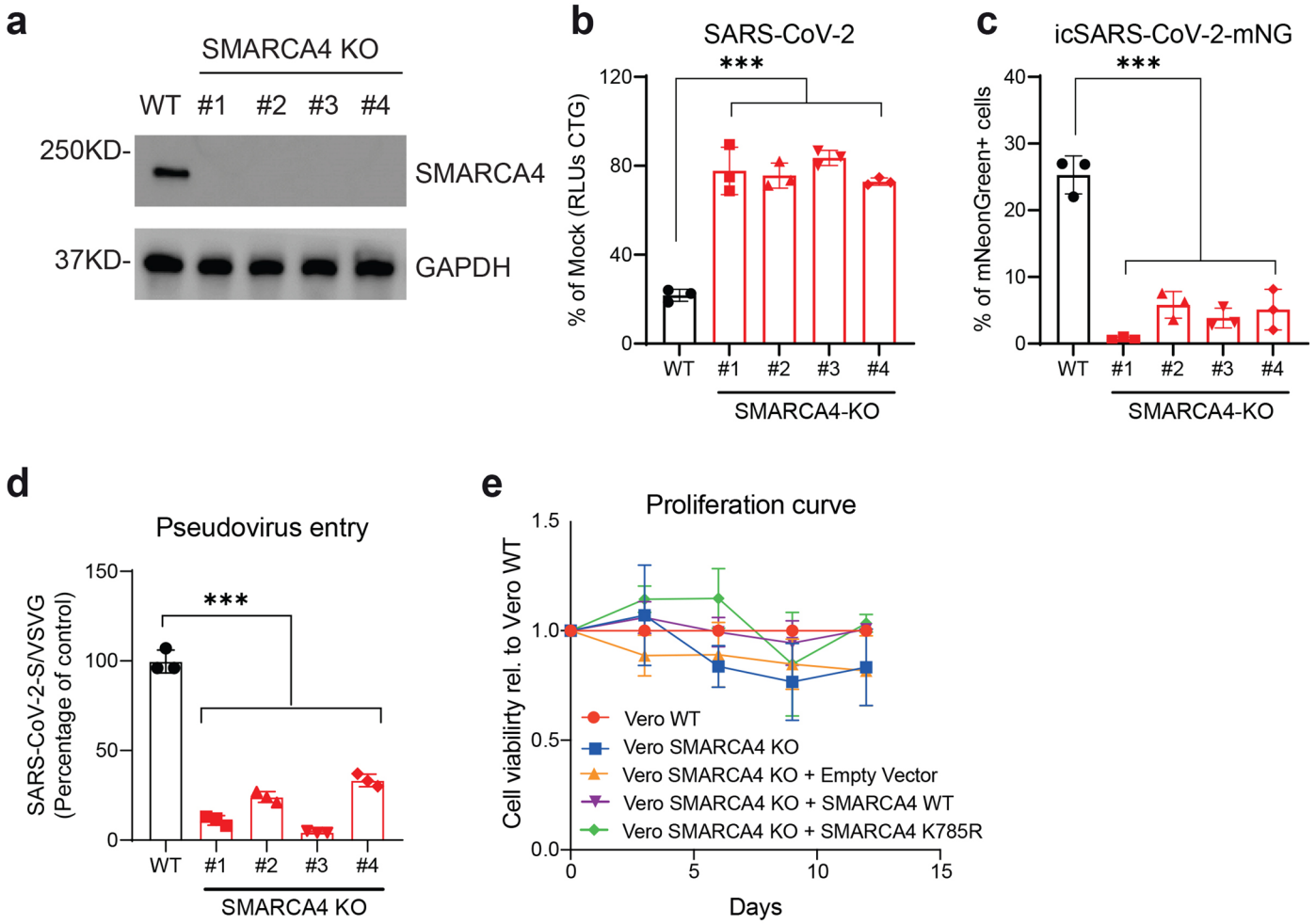

Extended Data Fig. 3 | SMARCA4 KO Vero E6 cells are resistant to SARS-CoV-2 infection. (a) CRISPR/Cas9-mediated SMARCA4 knockout was confirmed by immunoblot in Vero E6 cells. **(b)** Vero E6 cells were infected with SARS-CoV-2 at an MOI of 0.2. Cell viability relative to an uninfected control was measured 3 dpi with CellTiter Glo. **(c)** Vero E6 cells were infected with icSARS-CoV-2 mNG at an MOI of 1. Infected cell frequency was measured by mNeonGreen expression at 2 dpi. **(d)** SMARCA4 knockout Vero E6 cells were infected with VSV pseudovirus (VSVpp): VSVpp-VSV-G and VSVpp-SARS-CoV-2-S. Luciferase relative to a VSVpp-VSV-G control was measured 1 dpi. **(e)** Cell proliferation of Vero E6 wild type, SMARCA4 KO and KO rescued with empty vector, SMARCA4 wild type or K785R as measured using Cell Titer Glo. Shown are mean ± SEM. n = 3 biological replicates. Data in (a) is one representative one of three independent experiments. Data in (b-d) were analyzed by one-way ANOVA with Tukey's multiple comparison test. Shown are mean ± SEM. *$p < 0.05$, **$p < 0.01$, ***$p < 0.001$. n = 3 biological replicates.

https://doi.org/10.1038/s41588-023-01307-z

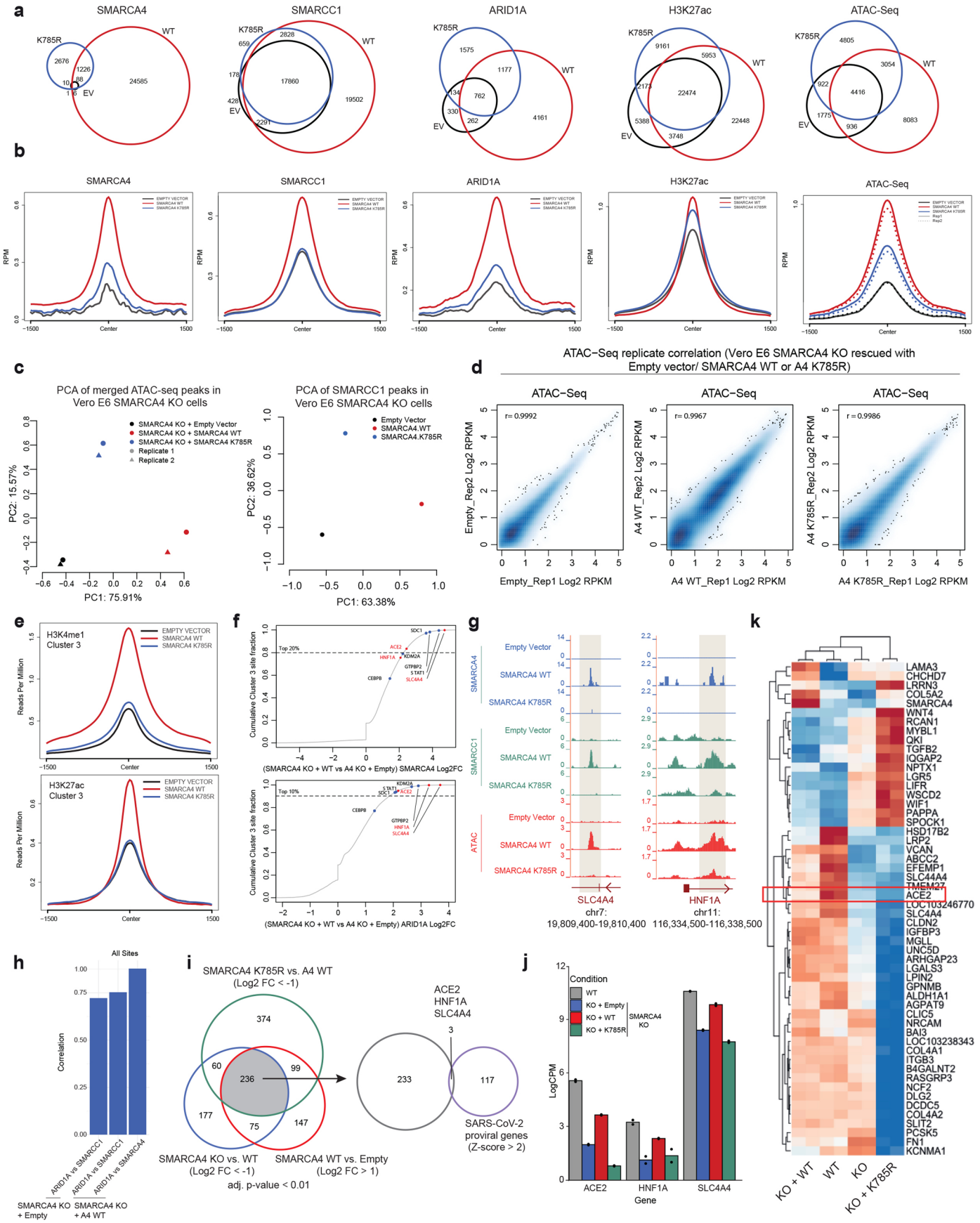

Extended Data Fig. 4 | See next page for caption.

https://doi.org/10.1038/s41588-023-01307-z

Extended Data Fig. 4 | ATPase-competent cBAF promotes ACE2 gene expression. (a) Venn diagrams depicting overlap of BAF subunit (SMARCA4, SMARCC1, ARID1A) or H3K27ac histone mark occupancy (CUT&Tag) and ATAC-Seq peaks in rescued SMARCA4 KO Vero E6 cells. **(b)** Metaplots of BAF subunit occupancy (SMARCA4, SMARCC1, ARID1A), H3K27ac histone mark, as measured by CUT&Tag, and ATAC-Seq peaks at all sites in rescued SMARCA4 KO Vero E6 cells. **(c)** PCA plots of merged SMARCC1 occupancy (CUT&Tag) (right) and ATAC-Seq (left) in rescued SMARCA4 KO Vero E6 cells **(d)** Scatter plots of ATAC-Seq replicates in SMARCA4 KO Vero E6 cells expressing Empty control, SMARCA4 WT and SMARCA4 K785R. The correlation coefficient 'r' is indicated (top left). **(e)** Metaplots of H3K4me1 and H3K27ac histone mark occupancy (CUT&Tag) at SMARCA4 WT-dependent sites (Cluster 3 from Fig. 2b). **(f)** Cumulative distribution function plots reflecting genes nearest to SMARCA4 and ARID1A gained sites in SMARCA4 KO cells rescued with SMARCA4 WT versus empty vector in Cluster 3 from Fig. 2b; top 1/10th or 1/20th fraction reflect genes associated with top-changed sites, sites highlighted in red indicate genes that scored as pro-viral determinants in CRISPR screen. **(g)** CUT&Tag and ATAC-Seq tracks at *SLC4A4* and *HNF1A* enhancers in rescued SMARCA4 KO Vero E6 cells. **(h)** Correlation between BAF subunit occupancies as profiled by CUT&Tag. **(i)** Venn diagram of overlap between ATPase-competent BAF-dependent transcripts (adj. p-value <0.01, calculated using EdgeR quasi-likelihood negative binomial generalized log-linear model, followed by Benjamini-Hochberg corrections) and proviral genes in the SARS-CoV-2 CRISPR screen (Z-score > 2). **(j)** RPKM levels of ACE2, HNF1A, and SLC4A4 in Vero E6 cells across indicated conditions (n = 2 biological replicates). **(k)** Heatmap of top differentially expressed genes (DEGs) in Vero E6 WT and SMARCA4 KO cells rescued with empty vector, SMARCA4 WT or SMARCA4 K785R. Red rectangle highlights ACE2.

https://doi.org/10.1038/s41588-023-01307-z

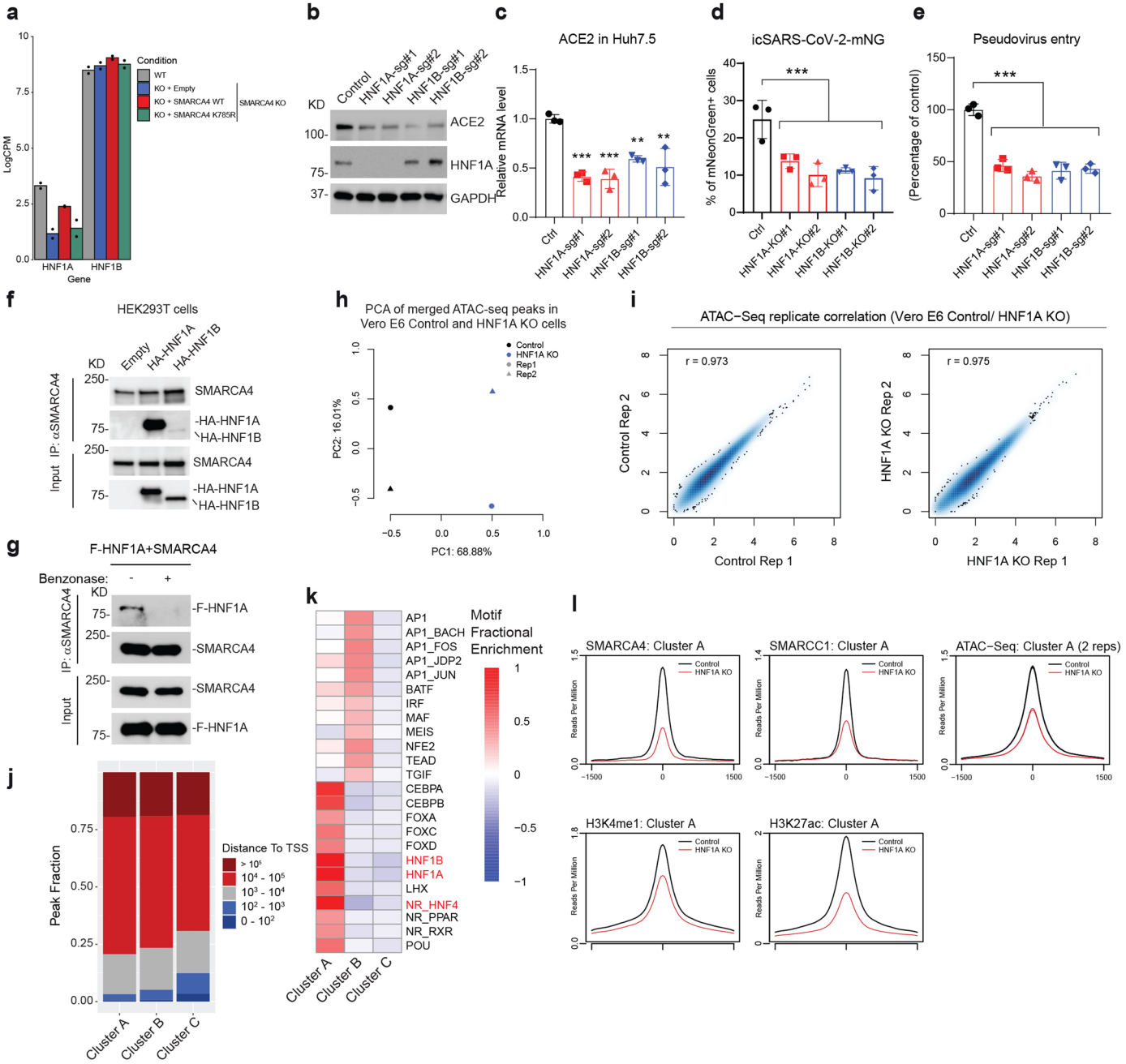

Extended Data Fig. 5 | HNF1A directs BAF complex targeting and regulates ACE2 expression. (a) RPKM levels for HNF1A and HNF1B in Vero E6 WT and SMARCA4 KO cells rescued with empty vector (Empty), SMARCA4 WT (A4 WT) or SMARCA4 K785R (A4 K785R) (n = 2 biological replicates). **(b-c)** ACE2 expression in HNF1A and HNF1B polyclonal KO Huh7.5 cells as measured by immunoblot (b) and RT-qPCR (c). **(d)** Huh7.5 cells were infected with icSARS-CoV-2-mNG at an MOI of 1. Infected cell frequency was measured by mNeonGreen expression at 2 dpi. **(e)** HNF1A and HNF1B polyclonal KO Huh7.5 cells were infected with VSV pseudovirus (VSVpp): VSVpp-VSV-G, VSVpp-SARS-CoV-2-S. Luciferase relative to the VSVpp-VSV-G control was measured 1 dpi. **(f)** Co-immunoprecipitation of SMARCA4 with HNF1A and HNF1B in HEK293T cells. **(g)** Co-immunoprecipitation of SMARCA4 with Flag-tagged HNF1A (F-HNF1A) in the presence of benzonase in HEK293T cells. **(h)** PCA plot of merged ATAC-Seq peaks in Vero E6 Control and HNF1A KO cells. **(i)** Scatter plots of ATAC-Seq replicates in Vero E6 Control and HNF1A KO cells. The correlation coefficient 'r' is indicated (top left). **(j)** Distance to TSS distribution of CUT&Tag and ATAC-Seq merged peaks for all conditions, across Clusters A-C in Vero E6 Control and HNF1A KO cells. **(k)** Heatmap depicting TF motif enrichment in Clusters A-C from Fig. 3j in Vero E6 Control and HNF1A KO cells. **(l)** Metaplots of SMARCA4, SMARCC1, H3K27ac and H3K4me1 chromatin occupancy (CUT&Tag) and DNA accessibility (ATAC-Seq) across Cluster A sites (lost sites) from Fig. 3j in Vero E6 Control and HNF1A KO cells. Data in (b, f-g) is one representative one of three independent experiments. Data in (c-e) were analyzed by one-way ANOVA with Tukey's multiple comparison test. Shown are mean ± SEM. *p < 0.05, **p < 0.01, ***p < 0.001, n = 3 biological replicates.

https://doi.org/10.1038/s41588-023-01307-z

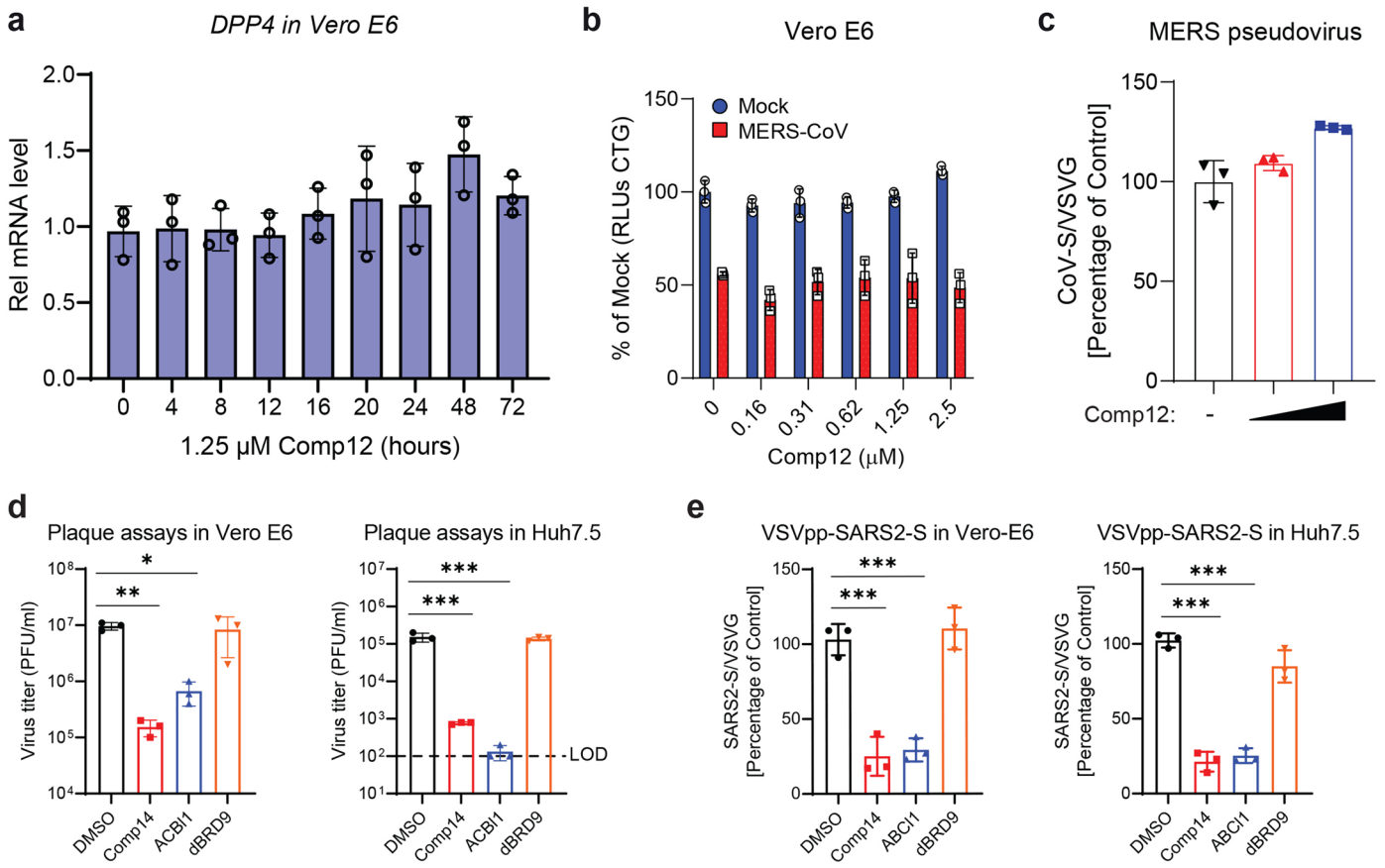

Extended Data Fig. 6 | Small molecule targeting of mSWI/SNF complexes inhibits SARS-CoV-2 but not MERS-CoV infection. (a) Vero E6 cells were treated with 1.25 μM Comp12 for the indicated times, DPP4 transcript level was measured by RT-qPCR. **(b)** Vero E6 cells were pretreated with Comp12 for 2 days and then infected with MERS-CoV at an MOI of 0.2. Cell viability relative to an uninfected control was measured 3 dpi with CellTiter Glo. **(c)** Vero E6 cells were pretreated with 1.25 or 2.5 μM Comp12 for 2 days and then infected with VSV pseudovirus (VSVpp): VSVpp-VSV-G, and VSVpp-MERS-S. Luciferase relative to a VSVpp-VSV-G control was measured 1 dpi. **(d)** Vero E6 and Huh7.5 cells were pre-treated with indicated inhibitors/degraders (2.5 μM) for 2 days prior to infecting with SARS-CoV-2. Virus replication was measured using plaque assay. Dash line, limit of detection. **(e)** Vero E6 and Huh7.5 cells were pre-treated with indicated inhibitors/degraders (2.5 μM) for 2 days prior to infecting with SARS-CoV-2 pseudovirus to assay for viral entry. Data in (a-e) were analyzed by one-way ANOVA with Tukey's multiple comparison test. Shown are mean ± SEM. *p < 0.05, **p < 0.01, ***p < 0.001, n = 3 biological replicates.

https://doi.org/10.1038/s41588-023-01307-z

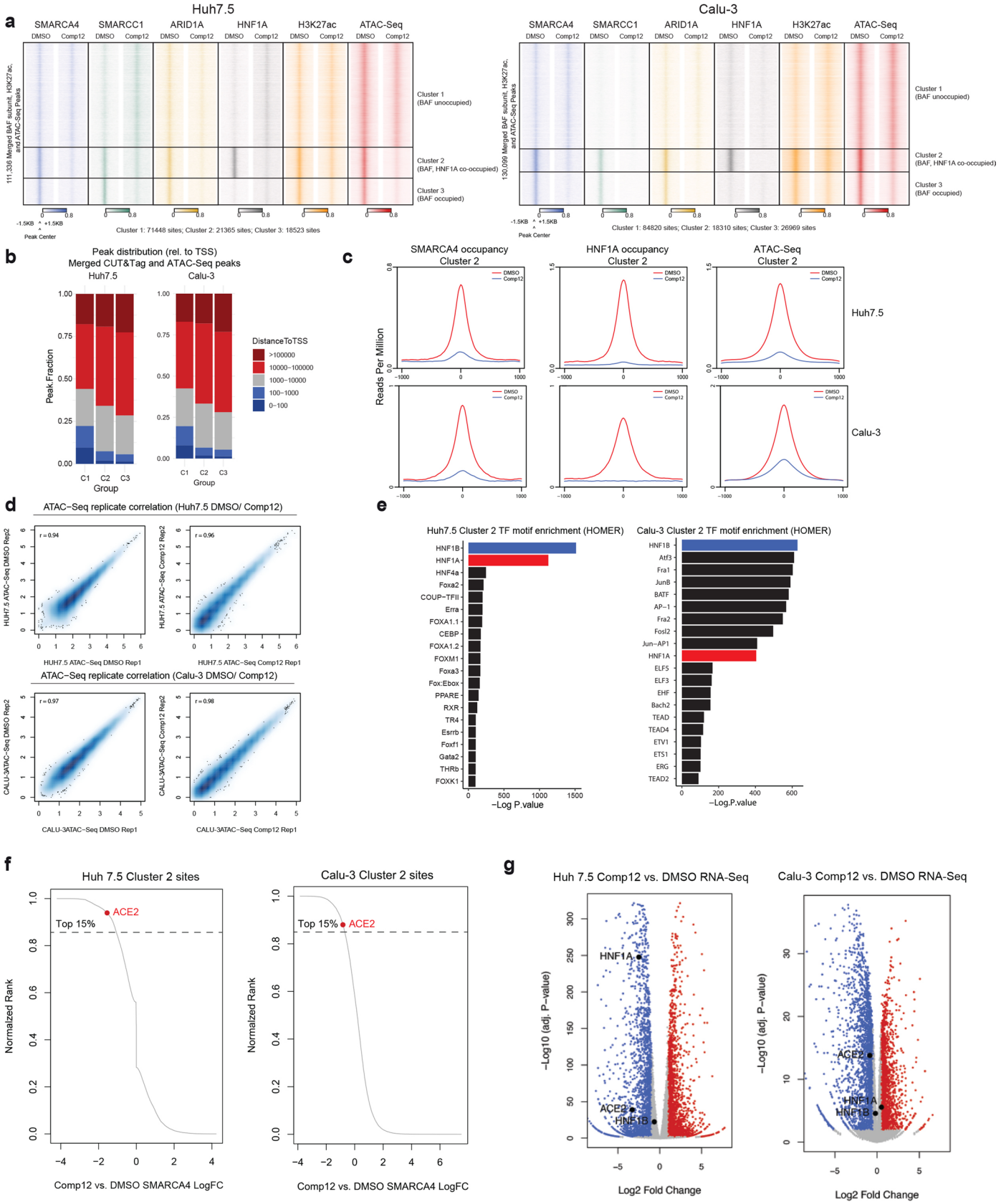

Extended Data Fig. 7 | See next page for caption.

https://doi.org/10.1038/s41588-023-01307-z

Extended Data Fig. 7 | HNF1A and cBAF regulate ACE2 expression in Huh7.5 and Calu-3 cells. (a) Heatmap and clustering analyses performed on merged BAF complex (SMARCA4, SMARCC1 and ARID1A), HNF1A, H3K27ac occupancies (n = 1), and ATAC-Seq (n = 2) peaks performed in Huh7.5 and Calu-3 cells treated with DMSO or 1.25 μM Comp12. **(b)** Distance to TSS distribution of CUT&Tag and ATAC-Seq merged peaks for all conditions, across Clusters 1-3 from (a). **(c)** Metaplots of SMARCA4, HNF1A occupancy (CUT&Tag) and ATAC-Seq peaks at BAF, HNF1A co-occupied sites (Cluster 2). **(d)** Scatter plots of ATAC-Seq replicates in DMSO and Comp12 treated cells. The correlation coefficient 'r' is indicated (top left). **(e)** Transcription factor motif enrichment analyses at BAF, HNF1A co-occupied sites (Cluster 2) (HOMER uses a binomial distribution to determine enrichment scores and p-values for known motifs). **(f)** Normalized rank of Cluster 2 sites plotted against SMARCA4 occupancy fold change after Comp12 treatment. **(g)** Volcano plots reflecting gene expression changes (RNA-Seq) between indicated conditions.The adj. p-value was calculated using EdgeR quasi-likelihood negative binomial generalized log-linear model, followed by Benjamini-Hochberg corrections.

https://doi.org/10.1038/s41588-023-01307-z

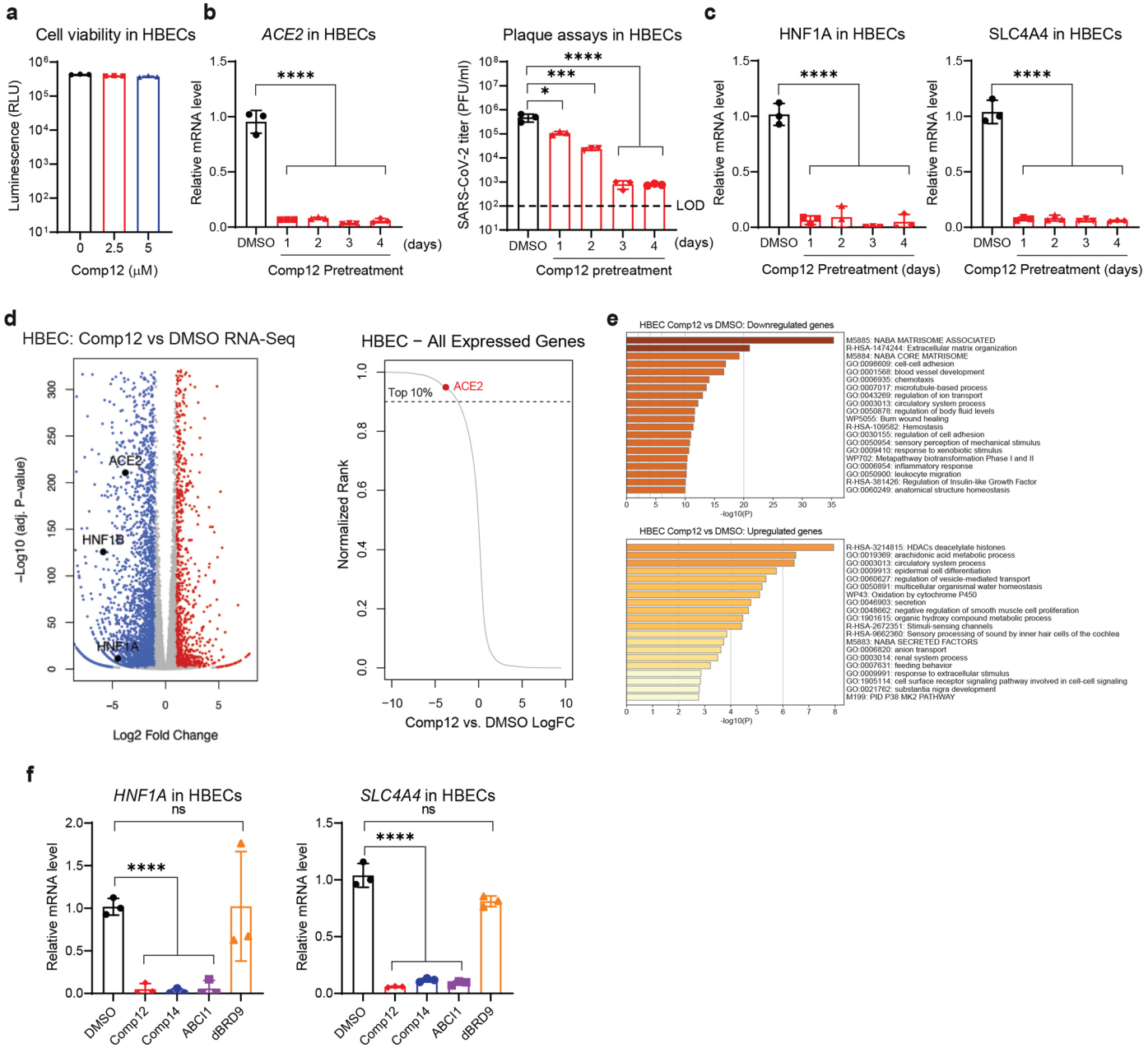

Extended Data Fig. 8 | Small molecule targeting of mSWI/SNF complexes in primary cells downregulates ACE2 expression. (a) Cell viability of HBECs after 4 days treatment of Comp12 at 2.5 and 5 μM. **(b)** HBECs were pre-treated with Comp12 for the indicated times, ACE2 expression was measured by RT-qPCR. HBECs were pre-treated with Comp12 for the indicated times and then infected with SARS-CoV-2 at an MOI of 0.5. Virus titer in the apical supernatant was measured by plaque assay. Dashed line, limit of detection. **(c)** HBECs were pre-treated with Comp12 at 2.5 μM for the indicated times, HNF1A and SLC4A4 expression was measured by RT-qPCR. **(d)** Volcano plots reflecting gene expression changes (RNA-seq) in HBECs after 4 days treatment of Comp12 at 2.5 μM. **(e)** Pathway analysis (Metascape) in Comp12 treated HBECs (n = 2 RNA-Seq biological replicates). P-values calculated using a hypergeometric test by Metascape. **(f)** HBECs were pretreated with the indicated inhibitors at 2.5 μM for 4 days, HNF1A and SLC4A4 expression were measured by RT-qPCR. Data in (a-c, f) were analyzed by one-way ANOVA with Tukey's multiple comparison test. Shown are mean ± SEM. *p < 0.05, **p < 0.01, ***p < 0.001, ****p < 0.0001, n = 3 biological replicates.

https://doi.org/10.1038/s41588-023-01307-z

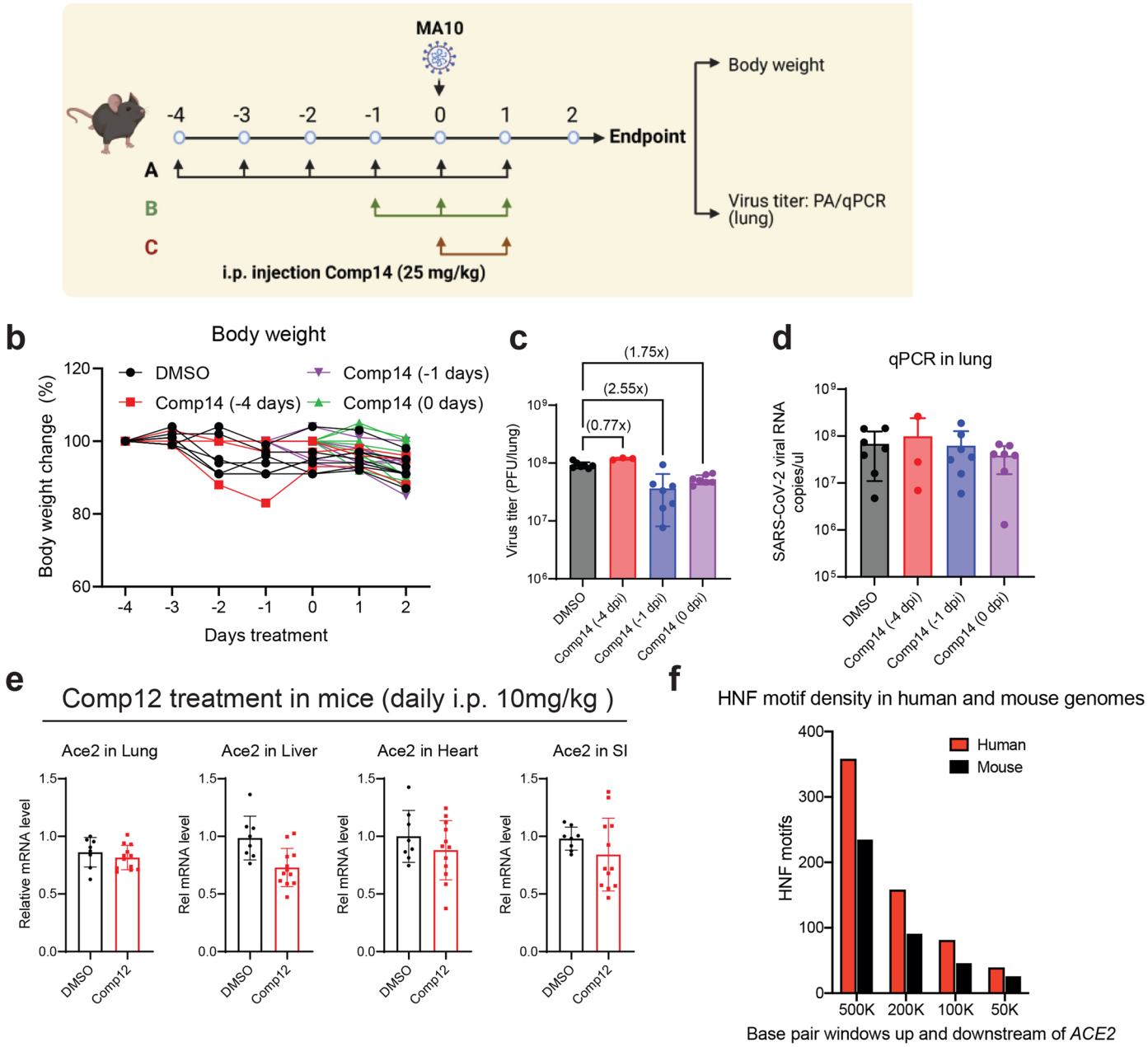

Extended Data Fig. 9 | BAF and HNF1A-mediated regulation of ACE2 expression and SARS-CoV-2 infection is not conserved in mice. (a) Schematic of Comp14 SMARCA4/2 ATPase inhibitor treatment (i.p. daily at 25 mg/kg) and virus infection in C57BL/6 J mice. **(b)** Body weight change of mice injected with Comp14 following the protocol outlined in (a). **(c, d)** SARS-CoV-2 MA10 virus titers (c) and viral genome levels (d) in lung tissues at 2 dpi. **(e)** C57BL/6 J mice were i.p. injected with Comp12 daily at 10 mg/Kg for 5 days and Ace2 expression in different tissues was measured by RT-qPCR. **(f)** HNF1 motif density around the ACE2 locus in human and mouse genomes. Data in (b-d) were analyzed by one-way ANOVA with Tukey's multiple comparison test. Shown are mean ± SEM. *p < 0.05, **p < 0.01, ***p < 0.001, n = 7 mice, or n = 3 mice. Data in (e) were analyzed by two-tailed t-test, n = 8 mice for DMSO, n = 12 mice for Comp12.

nature portfolio

Corresponding author(s): Craig Wilen

Last updated by author(s): Oct 14, 2022

Reporting Summary

Nature Portfolio wishes to improve the reproducibility of the work that we publish. This form provides structure for consistency and transparency in reporting. For further information on Nature Portfolio policies, see our Editorial Policies and the Editorial Policy Checklist.

Statistics

For all statistical analyses, confirm that the following items are present in the figure legend, table legend, main text, or Methods section.

n/a	Confirmed
☐	☒ The exact sample size (*n*) for each experimental group/condition, given as a discrete number and unit of measurement
☐	☒ A statement on whether measurements were taken from distinct samples or whether the same sample was measured repeatedly
☐	☒ The statistical test(s) used AND whether they are one- or two-sided *Only common tests should be described solely by name; describe more complex techniques in the Methods section.*
☒	☐ A description of all covariates tested
☒	☐ A description of any assumptions or corrections, such as tests of normality and adjustment for multiple comparisons
☐	☒ A full description of the statistical parameters including central tendency (e.g. means) or other basic estimates (e.g. regression coefficient) AND variation (e.g. standard deviation) or associated estimates of uncertainty (e.g. confidence intervals)
☐	☒ For null hypothesis testing, the test statistic (e.g. *F*, *t*, *r*) with confidence intervals, effect sizes, degrees of freedom and *P* value noted *Give P values as exact values whenever suitable.*
☒	☐ For Bayesian analysis, information on the choice of priors and Markov chain Monte Carlo settings
☒	☐ For hierarchical and complex designs, identification of the appropriate level for tests and full reporting of outcomes
☒	☐ Estimates of effect sizes (e.g. Cohen's *d*, Pearson's *r*), indicating how they were calculated

Our web collection on statistics for biologists contains articles on many of the points above.

Software and code

Policy information about availability of computer code

Data collection: All packages used for data analysis and collection are listed below in ChIP-seq section.

Data analysis	NGS Data Processing CUT&Tag, ATAC-Seq and human RNA-Seq samples were sequenced with the Illumina NextSeq 500 technology, and RNA-seq samples from Vero E6 cells were sequenced with Illumina NovaSeq 6000 technology. For the RNA-Seq data, reads were aligned to either the chlSab2 (NCBI annotation release 100) or the hg19 reference genome using STAR aligner v2.7.3a with parameters --winAnchorMultimapNmax 200 --outFilterMultimapNmax 100 --quantMode GeneCounts, and bigWig files were generated using the deeptools v3.1.3 bamCoverage function with the normalizeUsingRPKM option. Output gene count tables from STAR were used as input into the edgeR v3.12.1 R software package to evaluate differential gene expression. For ATAC-Seq data, read trimming was carried out by Trimmomatic v0.36, followed by alignment, duplicate read removal, and read quality filtering using Bowtie2, Picard v2.8.0 (http://broadinstitute.github.io/picard/), and SAMtools v 0.1.19, respectively, and ATAC-seq peaks were called with MACS2 v2.1 using the BAMPE option and a broad peak cutoff of 0.001. For ATAC-Seq track generation, output BAM files were converted into BigWig files using MACS2 and UCSC utilities in order to display coverage throughout the genome in RPM values. For CUT&Tag libraries, the CutRunTools pipeline was leveraged to perform read trimming, quality filtering, alignment, peak calling, and track building using default parameters. CUT&Tag and ATAC-seq Data Analyses Heatmaps and metaplots displaying signals aligned to peak centers were generated using ngsplot v2.63. K-means clustering was applied to output RPM values in order to partition the data into groups. The Bedtools multiIntersectBed and merge functions were used for peak merging, and distance-to-TSS peak distributions were computed utilizing Ensembl gene coordinates provided by the UCSC genome browser. Principle Component Analysis was performed using the wt.scale and fast.svd functions from the corpcor R package on log2-transformed RPKM values within merged peaks. Transcription factor motif positions within peaks were identified by the MEME FIMO v 4.12.0 software tool with position frequency matrices curated previously, and motif fractions of occurrence within clusters of peaks were computed using in-house scripts.

For manuscripts utilizing custom algorithms or software that are central to the research but not yet described in published literature, software must be made available to editors and reviewers. We strongly encourage code deposition in a community repository (e.g. GitHub). See the Nature Portfolio guidelines for submitting code & software for further information.

Data

Policy information about availability of data

All manuscripts must include a data availability statement. This statement should provide the following information, where applicable:

- Accession codes, unique identifiers, or web links for publicly available datasets
- A description of any restrictions on data availability
- For clinical datasets or third party data, please ensure that the statement adheres to our policy

All genomics data has been deposited under Gene Expression Omnibus GSE186201.

Field-specific reporting

Please select the one below that is the best fit for your research. If you are not sure, read the appropriate sections before making your selection.

☒ Life sciences ☐ Behavioural & social sciences ☐ Ecological, evolutionary & environmental sciences

For a reference copy of the document with all sections, see nature.com/documents/nr-reporting-summary-flat.pdf

Life sciences study design

All studies must disclose on these points even when the disclosure is negative.

Sample size	No sample-size calculations were performed, sample sizes were chosen based on the norm in the field of experimentation. All biochemical studies are performed in technical and experimental at least n>=3 replicates and genomic studies (ATAC,RNA) were carried out in duplicate across the cell lines and across multiple BAF subunits (one replicate each) for CUT&Tag studies, most appropriate for the evaluation of the biologic inquiries at hand.
Data exclusions	No data exclusions were conducted in this study.
Replication	All biochemical studies we were performed in triplicate (n=3) or greater for all experiments. Genomic studies from cell lines were all carried out in duplicate (ATAC, RNA) or probing mulitple BAF complex members independently (one replicate each) (CUT&Tag). All attempts at replication for data shown in the study were successful. Extensive measures were taken to verify reproducibility of results, including the utility of mutliple cell lines, where appropriate, multiple experiments performed by different individuals, and consistent validation of constructs used.
Randomization	Mice were randomized based on sex in the in vivo experiments, randomization was not required at any other stage of this study. Control of covariates was also not required since experiments performed were designed to measure the impact of genetic perturbations and small molecules across experimental conditions in cell lines or primary cells and not primary specimens or human patients.
Blinding	Blinding was not necessary in this study since it was not a clinical trial involving human patients. Investigators needed to have knowledge of the experimental groups and conditions.

Reporting for specific materials, systems and methods

We require information from authors about some types of materials, experimental systems and methods used in many studies. Here, indicate whether each material, system or method listed is relevant to your study. If you are not sure if a list item applies to your research, read the appropriate section before selecting a response.

Materials & experimental systems

n/a	Involved in the study
☐	☒ Antibodies
☐	☒ Eukaryotic cell lines
☒	☐ Palaeontology and archaeology
☐	☒ Animals and other organisms
☒	☐ Human research participants
☒	☐ Clinical data
☒	☐ Dual use research of concern

Methods

n/a	Involved in the study
☐	☒ ChIP-seq
☒	☐ Flow cytometry
☒	☐ MRI-based neuroimaging

Antibodies

Antibodies used

Antibody; Vendor; Catalog number; Application.
Anti-ACE2, ProSci, Cat#3217, Western blot: 1:2000
Anti-GAPDH antibody, BioLegend, Cat#607902, Western blot: 1:1000
Anti-LMNB1 antibody, BioLegend, Cat#869801, Western blot: 1:1000
Anti-Flag antibody, Sigma-Aldrich, Cat# F3165, Western blot: 1:1000
Anti-SMARCA4 antibody, Santa Cruz Biotechnology, Cat#sc-17796, Western blot: 1:2000, Co-IP: 1:200
Anti-SMARCA4 antibody, Cell Signaling Technology, Cat#49360, Western blot: 1:2000, CUT&Tag: 4uL/sample
Anti-SMARCC1 antibody, Cell Signaling Technology, Cat#11956, Western blot: 1:2000, CUT&Tag: 4uL/sample
Anti-ARID1A antibody, Cell Signaling Technology, Cat#12354, Western blot: 1:2000, CUT&Tag: 4uL/sample
Anti-H3K27ac antibody, Cell Signaling Technology, Cat#8173, CUT&Tag: 4uL/sample
Anti-H3K4me1 antibody, Abcam, Cat#ab176877, CUT&Tag: 0.5 ug/sample
Anti-HNF1A antibody, Abcam, Cat#ab272693, CUT&Tag: 0.5 ug/sample
Guinea Pig anti-Rabbit IgG, Antibodies-online, Cat#ABIN101961, CUT&Tag: 0.5 ug/sample
Anti-V5 antibody, Cell Signaling Technology, Cat#13202, Western blot: 1:1000, Co-IP:1:200
Anti-GAPDH, Santa Cruz Biotechnology, Cat#sc365062, Western blot: 1:5000
Anti-HNF1A antibody, Cell Signaling Technology, Cat# 89670, Western blot: 1:1000
Anti-HNF1B antibody, Thermo Fisher Scientific, Cat# 720259, Western blot: 1:1000
Anti-HA antibody, BioLegend, Cat# 901513, Western blot: 1:1000
Goat anti-mouse IgG antibody, IRDye 680RD conjugated, LI-COR Biosciences, Cat#926-68070, Western blot 1:10,000
Goat anti-rabbit IgG antibody, IRDye 800RD conjugated, LI-COR Biosciences, Cat#926-32211, Western blot 1:10,000
Goat anti-rabbit IgG/HRP, Jackson ImmunoResearch, Cat#111-035-003, Western blot 1:10,000
Goat anti-rat IgG/HRP, Jackson ImmunoResearch, Cat#112-035-003, Western blot 1:10,000
Goat anti-mouse IgG/HRP, Jackson ImmunoResearch, Cat#115-035-003, Western blot 1:10,000

Validation

All primary antibodies were validated in our laboratory for on-target specificity using cell lines in which the target was inactivated. These studies were performed in addition to the validation studies performed by the commercial vendor (use catalog numbers listed above to access this data on the websites of the vendors).

Eukaryotic cell lines

Policy information about cell lines

Cell line source(s)

HEK293T (ATCC, CRL-3216)
Vero E6 (ATCC, CRL-1586)
Huh7.5 (Washington University in St. Louis cell culture facility)
Calu-3 (ATCC, HTB-55)
HBEC (Lonza CC-2541)
H9 (WiCell)
Human Intestinal Enteroid (J2) (Texas Medical Center Digestive Diseases Center Enteroid Core).

Authentication

All cell lines were subjected to standard cell line fingerprinting analyses via our in-house cell line identify verification pipeline (Yale University and Dana-Farber Molecular Diagnostics Laboratory). ATCC performed STR profiling for HEK293T and Calu-3 cells. No Vero E6 or HBECs authentication was found on the vendors websites.

Mycoplasma contamination

All cell lines used in this study were routinely tested for mycoplasma contamination and were confirmed to be negative throughout the study.

Commonly misidentified lines
(See ICLAC register)

None of the cell lines used in this study are known to be commonly misidentified.

Animals and other organisms

Policy information about studies involving animals; ARRIVE guidelines recommended for reporting animal research

Laboratory animals	8–10 week old C57BL/6J mice (purchased from Jackson labs) of both genders were used in vivo experiments. All infections experiments were conducted in animal biosafety level 3 (ABSL-3) facilities at Yale University. All mice were housed in individually ventilated microisolator cages in a facility maintained at Yale University School of Medicine, on a 12 h light/dark cycle maintained at 40-60% humidity and 72 degrees F+/-2 degrees. Regular chow diet and water were given until the defined experimental endpoints. Researchers were not blinded during in vivo experiments.
Wild animals	No wild animals were used in this study
Field-collected samples	No field collected samples were used in this study
Ethics oversight	All animal work was approved by Institutional Animal Care and Use Committee (IACUC) at Yale University School of Medicine according to guidelines. All infection work was performed in an animal biosafety level 3 (ABSL-3) facility at Yale University School of Medicine.

Note that full information on the approval of the study protocol must also be provided in the manuscript.

ChIP-seq

Data deposition

☒ Confirm that both raw and final processed data have been deposited in a public database such as GEO.

☒ Confirm that you have deposited or provided access to graph files (e.g. BED files) for the called peaks.

Data access links *May remain private before publication.*	All genomics data has been deposited under GSE186201, https://www.ncbi.nlm.nih.gov/geo/query/acc.cgi?acc=GSE186201
Files in database submission	GSM5640292 ATACseq.VERO.HNF1AKO.Rep1 GSM5640293 ATACseq.VERO.HNF1AKO.Rep2 GSM5640294 ATACseq.VERO.LentiCRISPRv2.Control.Rep1 GSM5640295 ATACseq.VERO.LentiCRISPRv2.Control.Rep2 GSM5640296 ATACseq.VERO.SMARCA4KO.EmptyVector.Rep1 GSM5640297 ATACseq.VERO.SMARCA4KO.EmptyVector.Rep2 GSM5640298 ATACseq.VERO.SMARCA4KO.SMARCA4K785R.Rep1 GSM5640299 ATACseq.VERO.SMARCA4KO.SMARCA4K785R.Rep2 GSM5640300 ATACseq.VERO.SMARCA4KO.SMARCA4WT.Rep1 GSM5640301 ATACseq.VERO.SMARCA4KO.SMARCA4WT.Rep2 GSM5640302 CutAndTag.VERO.HNF1AKO.H3K27ac GSM5640303 CutAndTag.VERO.HNF1AKO.H3K4me1 GSM5640304 CutAndTag.VERO.HNF1AKO.SMARCA4 GSM5640305 CutAndTag.VERO.HNF1AKO.SMARCC1 GSM5640306 CutAndTag.VERO.LentiCRISPRv2.Control.H3K27ac GSM5640307 CutAndTag.VERO.LentiCRISPRv2.Control.H3K4me1 GSM5640308 CutAndTag.VERO.LentiCRISPRv2.Control.SMARCA4 GSM5640309 CutAndTag.VERO.LentiCRISPRv2.Control.SMARCC1 GSM5640310 CutAndTag.VERO.SMARCA4KO.EmptyVector.ARID1A GSM5640311 CutAndTag.VERO.SMARCA4KO.EmptyVector.H3K27ac GSM5640312 CutAndTag.VERO.SMARCA4KO.EmptyVector.H3K4me1 GSM5640313 CutAndTag.VERO.SMARCA4KO.EmptyVector.SMARCA4 GSM5640314 CutAndTag.VERO.SMARCA4KO.EmptyVector.SMARCC1 GSM5640315 CutAndTag.VERO.SMARCA4KO.SMARCA4K785R.ARID1A GSM5640316 CutAndTag.VERO.SMARCA4KO.SMARCA4K785R.H3K27ac GSM5640317 CutAndTag.VERO.SMARCA4KO.SMARCA4K785R.H3K4me1 GSM5640318 CutAndTag.VERO.SMARCA4KO.SMARCA4K785R.SMARCA4 GSM5640319 CutAndTag.VERO.SMARCA4KO.SMARCA4K785R.SMARCC1 GSM5640320 CutAndTag.VERO.SMARCA4KO.SMARCA4WT.ARID1A GSM5640321 CutAndTag.VERO.SMARCA4KO.SMARCA4WT.H3K27ac GSM5640322 CutAndTag.VERO.SMARCA4KO.SMARCA4WT.H3K4me1 GSM5640323 CutAndTag.VERO.SMARCA4KO.SMARCA4WT.SMARCA4 GSM5640324 CutAndTag.VERO.SMARCA4KO.SMARCA4WT.SMARCC1 GSM5640325 RNAseq.VERO.SMARCA4KO.EmptyVector.Rep1 GSM5640326 RNAseq.VERO.SMARCA4KO.EmptyVector.Rep2 GSM5640327 RNAseq.VERO.SMARCA4KO.SMARCA4K785R.Rep1 GSM5640328 RNAseq.VERO.SMARCA4KO.SMARCA4K785R.Rep2 GSM5640329 RNAseq.VERO.SMARCA4KO.SMARCA4WT.Rep1 GSM5640330 RNAseq.VERO.SMARCA4KO.SMARCA4WT.Rep2 GSM5640331 RNAseq.VERO.WT.Rep1 GSM5640332 RNAseq.VERO.WT.Rep2 GSM6254270 ATACseq.CALU3.C12.Rep1 GSM6254271 ATACseq.CALU3.C12.Rep2

GSM6254272 ATACseq.CALU3.DMSO.Rep1
GSM6254273 ATACseq.CALU3.DMSO.Rep2
GSM6254274 ATACseq.HUH7.C12.Rep1
GSM6254275 ATACseq.HUH7.C12.Rep2
GSM6254276 ATACseq.HUH7.DMSO.Rep1
GSM6254277 ATACseq.HUH7.DMSO.Rep2
GSM6254278 CutAndTag.CALU3.C12.ARID1A
GSM6254279 CutAndTag.CALU3.C12.H3K27ac
GSM6254280 CutAndTag.CALU3.C12.HNF1A
GSM6254281 CutAndTag.CALU3.C12.IgG
GSM6254282 CutAndTag.CALU3.C12.SMARCA4
GSM6254283 CutAndTag.CALU3.C12.SMARCC1
GSM6254284 CutAndTag.CALU3.DMSO.ARID1A
GSM6254285 CutAndTag.CALU3.DMSO.H3K27ac
GSM6254286 CutAndTag.CALU3.DMSO.HNF1A
GSM6254287 CutAndTag.CALU3.DMSO.IgG
GSM6254288 CutAndTag.CALU3.DMSO.SMARCA4
GSM6254289 CutAndTag.CALU3.DMSO.SMARCC1
GSM6254290 CutAndTag.HUH7.C12.ARID1A
GSM6254291 CutAndTag.HUH7.C12.H3K27ac
GSM6254292 CutAndTag.HUH7.C12.HNF1A
GSM6254293 CutAndTag.HUH7.C12.IgG
GSM6254294 CutAndTag.HUH7.C12.SMARCA4
GSM6254295 CutAndTag.HUH7.C12.SMARCC1
GSM6254296 CutAndTag.HUH7.DMSO.ARID1A
GSM6254297 CutAndTag.HUH7.DMSO.H3K27ac
GSM6254298 CutAndTag.HUH7.DMSO.HNF1A
GSM6254299 CutAndTag.HUH7.DMSO.IgG
GSM6254300 CutAndTag.HUH7.DMSO.SMARCA4
GSM6254301 CutAndTag.HUH7.DMSO.SMARCC1
GSM6254302 RNAseq.CALU3.C12.Rep1
GSM6254303 RNAseq.CALU3.C12.Rep2
GSM6254304 RNAseq.CALU3.DMSO.Rep1
GSM6254305 RNAseq.CALU3.DMSO.Rep2
GSM6254306 RNAseq.HBEC.C12.Rep1
GSM6254307 RNAseq.HBEC.C12.Rep2
GSM6254308 RNAseq.HBEC.DMSO.Rep1
GSM6254309 RNAseq.HBEC.DMSO.Rep2
GSM6254310 RNAseq.HUH7.C12.Rep1
GSM6254311 RNAseq.HUH7.C12.Rep2
GSM6254312 RNAseq.HUH7.DMSO.Rep1
GSM6254313 RNAseq.HUH7.DMSO.Rep2

Genome browser session
(e.g. UCSC)

N/A

Methodology

Replicates

All ATAC-Seq and RNA-seq experiments were performed with at least two experimental replicates.

Sequencing depth

Sample ;Raw; Mapped; Uniquely Mapped; Length; Type
ATACseq.VERO.SMARCA4KO.EmptyVector.Rep1 50064446 47960635 18811100 35 Paired-End
ATACseq.VERO.SMARCA4KO.EmptyVector.Rep2 54553022 52199365 21231096 35 Paired-End
ATACseq.VERO.SMARCA4KO.SMARCA4WT.Rep1 97178490 93511756 21931011 35 Paired-End
ATACseq.VERO.SMARCA4KO.SMARCA4WT.Rep2 48942350 47275025 12850909 35 Paired-End
ATACseq.VERO.SMARCA4KO.SMARCA4K785R.Rep1 46208267 44452426 12905870 35 Paired-End
ATACseq.VERO.SMARCA4KO.SMARCA4K785R.Rep2 53378858 51234025 16266283 35 Paired-End
ATACseq.VERO.LentiCRISPRv2.Control.Rep1 40703413 39303072 27152478 35 Paired-End
ATACseq.VERO.LentiCRISPRv2.Control.Rep2 46296458 44684410 32434560 35 Paired-End
ATACseq.VERO.HNF1AKO.Rep1 50040529 48183631 34580401 35 Paired-End
ATACseq.VERO.HNF1AKO.Rep2 35637193 34419439 25112053 35 Paired-End
CutAndTag.VERO.LentiCRISPRv2.Control.SMARCA4 15843744 15151271 3598525 35 Paired-End
CutAndTag.VERO.LentiCRISPRv2.Control.SMARCC1 1641509 1577751 987386 35 Paired-End
CutAndTag.VERO.LentiCRISPRv2.Control.H3K27ac 21821593 21181148 16267911 35 Paired-End
CutAndTag.VERO.LentiCRISPRv2.Control.H3K4me1 36782896 35501871 29345293 35 Paired-End
CutAndTag.VERO.HNF1AKO.SMARCA4 7600038 7262921 2276367 35 Paired-End
CutAndTag.VERO.HNF1AKO.SMARCC1 11897081 11406285 5600223 35 Paired-End
CutAndTag.VERO.HNF1AKO.H3K27ac 25502037 24727475 18616363 35 Paired-End
CutAndTag.VERO.HNF1AKO.H3K4me1 37867845 36540432 30818736 35 Paired-End
CutAndTag.VERO.SMARCA4KO.EmptyVector.SMARCA4 83033 74900 54129 35 Paired-End
CutAndTag.VERO.SMARCA4KO.SMARCA4WT.SMARCA4 8470011 8009993 2821037 35 Paired-End
CutAndTag.VERO.SMARCA4KO.SMARCA4K785R.SMARCA4 711296 668318 334248 35 Paired-End
CutAndTag.VERO.SMARCA4KO.EmptyVector.SMARCC1 8924313 8378840 5050556 35 Paired-End
CutAndTag.VERO.SMARCA4KO.EmptyVector.ARID1A 10483042 9948455 2529762 35 Paired-End
CutAndTag.VERO.SMARCA4KO.EmptyVector.H3K27ac 8760810 8440780 7779031 35 Paired-End
CutAndTag.VERO.SMARCA4KO.EmptyVector.H3K4me1 9679958 9418710 8480066 35 Paired-End

CutAndTag.VERO.SMARCA4KO.SMARCA4WT.SMARCC1 10070988 9476553 3780608 35 Paired-End
CutAndTag.VERO.SMARCA4KO.SMARCA4WT.ARID1A 10177954 9478853 1929227 35 Paired-End
CutAndTag.VERO.SMARCA4KO.SMARCA4WT.H3K27ac 10034560 9651293 8358126 35 Paired-End
CutAndTag.VERO.SMARCA4KO.SMARCA4WT.H3K4me1 11494931 10863752 9330520 35 Paired-End
CutAndTag.VERO.SMARCA4KO.SMARCA4K785R.SMARCC1 9763351 9214464 6155927 35 Paired-End
CutAndTag.VERO.SMARCA4KO.SMARCA4K785R.ARID1A 12028716 11281821 2983073 35 Paired-End
CutAndTag.VERO.SMARCA4KO.SMARCA4K785R.H3K27ac 10135395 9716169 8669656 35 Paired-End
CutAndTag.VERO.SMARCA4KO.SMARCA4K785R.H3K4me1 11735226 11321496 10337708 35 Paired-End
RNAseq.VERO.SMARCA4KO.EmptyVector.Rep1 34972676 32117051 30588498 195 Paired-End
RNAseq.VERO.SMARCA4KO.EmptyVector.Rep2 39372910 37047505 34781556 195 Paired-End
RNAseq.VERO.SMARCA4KO.SMARCA4K785R.Rep1 41272795 38920061 37201048 195 Paired-End
RNAseq.VERO.SMARCA4KO.SMARCA4K785R.Rep2 35911806 34089197 32522672 195 Paired-End
RNAseq.VERO.SMARCA4KO.SMARCA4WT.Rep1 29688599 27850389 26549323 195 Paired-End
RNAseq.VERO.SMARCA4KO.SMARCA4WT.Rep2 37186405 35158173 33428929 195 Paired-End
RNAseq.VERO.WT.Rep1 35001460 33276812 31937466 195 Paired-End
RNAseq.VERO.WT.Rep2 30525617 28792825 27513620 195 Paired-End
ATACseq.HUH7.DMSO.Rep1 73552084 72910492 39745383 35 Paired-End
ATACseq.HUH7.DMSO.Rep2 94977254 94074492 50054494 35 Paired-End
ATACseq.HUH7.C12.Rep1 114859074 113578633 56233500 35 Paired-End
ATACseq.HUH7.C12.Rep2 71218896 70661392 33309222 35 Paired-End
ATACseq.CALU3.DMSO.Rep1 104751662 103861624 82231751 35 Paired-End
ATACseq.CALU3.DMSO.Rep2 95012850 94174177 76705963 35 Paired-End
ATACseq.CALU3.C12.Rep1 86556466 85804953 70609291 35 Paired-End
ATACseq.CALU3.C12.Rep2 108666628 107456305 89666621 35 Paired-End
CutAndTag.HUH7.DMSO.SMARCA4 5085029 4918511 2425331 35 Paired-End
CutAndTag.HUH7.DMSO.ARID1A 5663126 5461988 2475931 35 Paired-End
CutAndTag.HUH7.DMSO.SMARCC1 2241316 2169597 1248939 35 Paired-End
CutAndTag.HUH7.DMSO.HNF1A 3532572 3400988 1300143 35 Paired-End
CutAndTag.HUH7.DMSO.H3K27ac 25896526 25562504 20723209 35 Paired-End
CutAndTag.HUH7.DMSO.IgG 26795 25815 17162 35 Paired-End
CutAndTag.HUH7.C12.SMARCA4 5325436 5113629 2462887 35 Paired-End
CutAndTag.HUH7.C12.ARID1A 6005413 5783054 3432016 35 Paired-End
CutAndTag.HUH7.C12.SMARCC1 8836719 8527034 3725423 35 Paired-End
CutAndTag.HUH7.C12.HNF1A 12455961 12037067 5292795 35 Paired-End
CutAndTag.HUH7.C12.H3K27ac 17183864 16936723 12582524 35 Paired-End
CutAndTag.HUH7.C12.IgG 31809 30732 20404 35 Paired-End
CutAndTag.CALU3.DMSO.SMARCA4 7296925 7117743 2772901 35 Paired-End
CutAndTag.CALU3.DMSO.ARID1A 4461567 4357105 1900877 35 Paired-End
CutAndTag.CALU3.DMSO.SMARCC1 931569 907737 636903 35 Paired-End
CutAndTag.CALU3.DMSO.HNF1A 4671727 4479874 1838186 35 Paired-End
CutAndTag.CALU3.DMSO.H3K27ac 22349971 22105999 15002181 35 Paired-End
CutAndTag.CALU3.DMSO.IgG 7712 7494 6493 35 Paired-End
CutAndTag.CALU3.C12.SMARCA4 5154448 4980944 1547165 35 Paired-End
CutAndTag.CALU3.C12.ARID1A 2547564 2443563 1005072 35 Paired-End
CutAndTag.CALU3.C12.SMARCC1 844705 817911 466813 35 Paired-End
CutAndTag.CALU3.C12.HNF1A 3007548 2911133 1528035 35 Paired-End
CutAndTag.CALU3.C12.H3K27ac 17481621 17242408 11051405 35 Paired-End
CutAndTag.CALU3.C12.IgG 9045 7855 6349 35 Paired-End
RNAseq.HUH7.DMSO.Rep1 27473853 27281475 21718543 75 Single-End
RNAseq.HUH7.DMSO.Rep2 30866627 30665354 24449432 75 Single-End
RNAseq.HUH7.C12.Rep1 27881121 27685709 21158144 75 Single-End
RNAseq.HUH7.C12.Rep2 31563767 31340468 23870488 75 Single-End
RNAseq.CALU3.DMSO.Rep1 32724097 32471665 24937325 75 Single-End
RNAseq.CALU3.DMSO.Rep2 33967040 33707698 25763308 75 Single-End
RNAseq.CALU3.C12.Rep1 30218878 29987337 22481939 75 Single-End
RNAseq.CALU3.C12.Rep2 30671807 30430405 22859537 75 Single-End
RNAseq.HBEC.DMSO.Rep1 37562554 37276351 28924591 75 Single-End
RNAseq.HBEC.DMSO.Rep2 32775690 32525618 25390844 75 Single-End
RNAseq.HBEC.C12.Rep1 32092433 31869140 24173958 75 Single-End
RNAseq.HBEC.C12.Rep2 38469728 38223369 29057408 75 Single-End

Antibodies

Antibody for CUT&Tag; Vendor; Catalog number; Lot number
anti-SMARCA4 (Cell Signaling Technology Catalog#: 41360 Lot:3),
anti-ARID1A (Cell Signaling Technology Catalog#: 12354 Lot:3),
anti-SMARCC1 (Cell Signaling Technology Catalog#: 11956 Lot:4),
anti-H3K27ac (Cell Signaling Technology Catalog#: 8173 Lot:6),
anti-H3K4me1 (Abcam Catalog#: ab176877 Lot:GR208955-5)

Peak calling parameters

For ATAC-Seq data, read trimming was carried out by Trimmomatic v0.36, followed by alignment, duplicate read removal, and read quality filtering using Bowtie2, Picard v2.8.0, and SAMtools v 0.1.19, respectively. ATAC-seq peaks were called with MACS2 v2.1 using the BAMPE option and a broad peak cutoff of 0.001. For CUT&Tag libraries, the CutRunTools pipeline was leveraged to perform read trimming, quality filtering, alignment, duplicate read removal, peak calling, and track building using default parameters. From this pipeline, we used narrow peaks called by MACS2 with a q-value cutoff of 0.01. For the RNA-Seq data, reads were aligned to either the chlSab2 (NCBI annotation release 100) or the hg19 reference genome using STAR aligner v2.7.3a with parameters --winAnchorMultimapNmax 200 --outFilterMultimapNmax 100 --quantMode GeneCounts, and bigWig files were generated using the

deeptools v3.1.3 bamCoverage function with the normalizeUsingRPKM option. Output gene count tables from STAR were used as input into the edgeR v3.12.1 R software package to evaluate differential gene expression.

Data quality

Sample	Peak.Count
ATACseq.VERO.SMARCA4KO.EmptyVector.Rep1	21276
ATACseq.VERO.SMARCA4KO.EmptyVector.Rep2	22174
ATACseq.VERO.SMARCA4KO.SMARCA4WT.Rep1	42491
ATACseq.VERO.SMARCA4KO.SMARCA4WT.Rep2	32296
ATACseq.VERO.SMARCA4KO.SMARCA4K785R.Rep1	21693
ATACseq.VERO.SMARCA4KO.SMARCA4K785R.Rep2	23110
ATACseq.VERO.LentiCRISPRv2.Control.Rep1	63567
ATACseq.VERO.LentiCRISPRv2.Control.Rep2	71290
ATACseq.VERO.HNF1AKO.Rep1	70060
ATACseq.VERO.HNF1AKO.Rep2	58042
CutAndTag.VERO.LentiCRISPRv2.Control.SMARCA4	23243
CutAndTag.VERO.LentiCRISPRv2.Control.SMARCC1	11860
CutAndTag.VERO.LentiCRISPRv2.Control.H3K27ac	70129
CutAndTag.VERO.LentiCRISPRv2.Control.H3K4me1	165824
CutAndTag.VERO.HNF1AKO.SMARCA4	22895
CutAndTag.VERO.HNF1AKO.SMARCC1	28224
CutAndTag.VERO.HNF1AKO.H3K27ac	67782
CutAndTag.VERO.HNF1AKO.H3K4me1	173560
CutAndTag.VERO.SMARCA4KO.EmptyVector.SMARCA4	119
CutAndTag.VERO.SMARCA4KO.SMARCA4WT.SMARCA4	25905
CutAndTag.VERO.SMARCA4KO.SMARCA4K785R.SMARCA4	4049
CutAndTag.VERO.SMARCA4KO.EmptyVector.SMARCC1	8072
CutAndTag.VERO.SMARCA4KO.EmptyVector.ARID1A	1502
CutAndTag.VERO.SMARCA4KO.EmptyVector.H3K27ac	35055
CutAndTag.VERO.SMARCA4KO.EmptyVector.H3K4me1	76005
CutAndTag.VERO.SMARCA4KO.SMARCA4WT.SMARCC1	16538
CutAndTag.VERO.SMARCA4KO.SMARCA4WT.ARID1A	6369
CutAndTag.VERO.SMARCA4KO.SMARCA4WT.H3K27ac	56642
CutAndTag.VERO.SMARCA4KO.SMARCA4WT.H3K4me1	53281
CutAndTag.VERO.SMARCA4KO.SMARCA4K785R.SMARCC1	13239
CutAndTag.VERO.SMARCA4KO.SMARCA4K785R.ARID1A	3662
CutAndTag.VERO.SMARCA4KO.SMARCA4K785R.H3K27ac	40032
CutAndTag.VERO.SMARCA4KO.SMARCA4K785R.H3K4me1	74073
ATACseq.CALU3.C12.Rep1.broadPeak	52932
ATACseq.CALU3.C12.Rep2.broadPeak	56324
ATACseq.CALU3.DMSO.Rep1.broadPeak	90676
ATACseq.CALU3.DMSO.Rep2.broadPeak	87435
ATACseq.HUH7.C12.Rep1.broadPeak	25955
ATACseq.HUH7.C12.Rep2.broadPeak	22498
ATACseq.HUH7.DMSO.Rep1.broadPeak	52593
ATACseq.HUH7.DMSO.Rep2.broadPeak	56964
CutAndTag.CALU3.C12.ARID1A.narrowPeak	3271
CutAndTag.CALU3.C12.H3K27ac.narrowPeak	34824
CutAndTag.CALU3.C12.HNF1A.narrowPeak	445
CutAndTag.CALU3.C12.IgG.narrowPeak	0
CutAndTag.CALU3.C12.SMARCA4.narrowPeak	7773
CutAndTag.CALU3.C12.SMARCC1.narrowPeak	301
CutAndTag.CALU3.DMSO.ARID1A.narrowPeak	14917
CutAndTag.CALU3.DMSO.H3K27ac.narrowPeak	53863
CutAndTag.CALU3.DMSO.HNF1A.narrowPeak	3287
CutAndTag.CALU3.DMSO.IgG.narrowPeak	0
CutAndTag.CALU3.DMSO.SMARCA4.narrowPeak	20035
CutAndTag.CALU3.DMSO.SMARCC1.narrowPeak	1444
CutAndTag.HUH7.C12.ARID1A.narrowPeak	1982
CutAndTag.HUH7.C12.H3K27ac.narrowPeak	45330
CutAndTag.HUH7.C12.HNF1A.narrowPeak	5088
CutAndTag.HUH7.C12.IgG.narrowPeak	1
CutAndTag.HUH7.C12.SMARCA4.narrowPeak	3272
CutAndTag.HUH7.C12.SMARCC1.narrowPeak	7484
CutAndTag.HUH7.DMSO.ARID1A.narrowPeak	10897
CutAndTag.HUH7.DMSO.H3K27ac.narrowPeak	76144
CutAndTag.HUH7.DMSO.HNF1A.narrowPeak	7662
CutAndTag.HUH7.DMSO.IgG.narrowPeak	2
CutAndTag.HUH7.DMSO.SMARCA4.narrowPeak	12134
CutAndTag.HUH7.DMSO.SMARCC1.narrowPeak	6136

Software

NGS Data Processing
CUT&Tag, ATAC-Seq and human RNA-Seq samples were sequenced with the Illumina NextSeq 500 technology, and RNA-seq samples from Vero E6 cells were sequenced with Illumina NovaSeq 6000 technology. For the RNA-Seq data, reads were aligned to either the chlSab2 (NCBI annotation release 100) or the hg19 reference genome using STAR aligner v2.7.3a with parameters --winAnchorMultimapNmax 200 --outFilterMultimapNmax 100 --quantMode GeneCounts, and bigWig files were generated using the deeptools v3.1.3 bamCoverage function with the normalizeUsingRPKM option. Output gene count tables from STAR were used as

input into the edgeR v3.12.1 R software package to evaluate differential gene expression. For ATAC-Seq data, read trimming was carried out by Trimmomatic v0.36, followed by alignment, duplicate read removal, and read quality filtering using Bowtie2, Picard v2.8.0 (http://broadinstitute.github.io/picard/), and SAMtools v 0.1.19, respectively, and ATAC-seq peaks were called with MACS2 v2.1 using the BAMPE option and a broad peak cutoff of 0.001. For ATAC-Seq track generation, output BAM files were converted into BigWig files using MACS2 and UCSC utilities in order to display coverage throughout the genome in RPM values. For Cut and Tag libraries, the CutRunTools pipeline was leveraged to perform read trimming, quality filtering, alignment, peak calling, and track building using default parameters.

CUT&Tag and ATAC-seq Data Analyses

Heatmaps and metaplots displaying signals aligned to peak centers were generated using ngsplot v2.63. K-means clustering was applied to output RPM values in order to partition the data into groups. The Bedtools multiIntersectBed and merge functions were used for peak merging, and distance-to-TSS peak distributions were computed utilizing Ensembl gene coordinates provided by the UCSC genome browser. Principle Component Analysis was performed using the wt.scale and fast.svd functions from the corpcor R package on log2-transformed RPKM values within merged peaks. Transcription factor motif positions within peaks were identified by the MEME FIMO v 4.12.0 software tool with position frequency matrices curated previously, and motif fractions of occurrence within clusters of peaks were computed using in-house scripts.